POLYMER-DISPERSED LIQUID CRYSTAL ELASTOMERS

Andraž Rešetič

Doctoral Dissertation
Jožef Stefan International Postgraduate School
Ljubljana, Slovenia

Supervisor: Prof. Dr. Boštjan Zalar, Jožef Stefan International Postgraduate School, Jamova 39, 1000 Ljubljana, Slovenia

Evaluation Board:
Prof. Dr. Zdravko Kutnjak, Chairman, Jožef Stefan Institute, Jamova 39, 1000 Ljubljana, Slovenia
Doc. Dr. Tomaž Apih, Member, Jožef Stefan Institute, Jamova 39, 1000 Ljubljana, Slovenia
Dr. Valentina Domenici, Member, Dipartimento di Chimica e Chimica Industriale, Università degli studi di Pisa, via Moruzzi 13, 56124 Pisa, Italy

MEDNARODNA PODIPLOMSKA ŠOLA JOŽEFA STEFANA
JOŽEF STEFAN INTERNATIONAL POSTGRADUATE SCHOOL



Andraž Rešetič

POLYMER-DISPERSED LIQUID CRYSTAL ELASTOMERS

Doctoral Dissertation

POLIMERNO DISPERGIRANI TEKOČEKRISTALNI ELASTOMERI

Doktorska disertacija

Supervisor: Prof. Dr. Boštjan Zalar

Ljubljana, Slovenia, December 2016

Acknowledgments

I would like to thank my advisor Prof. Dr. Boštjan Zalar for his invaluable and patient support during my Ph.D. studies and for introducing me to the interesting field of liquid crystal elastomers and experimental NMR.

Special thanks goes to all the people of the 'Pod smreko' team, Jerneja Milavec, Blaž Zupančič and Valentina Domenici, for all the helpful advice, shared ideas and help during my laboratory work, and also for making those long hours in the lab considerably shorter and fun.

I would also like to express my gratitude to all the members of the Department of Condesed Matter Physics – F5, at the J. Stefan Institute for all their knowledge and help given in the course of my work, and for all the fun conversations held in the department corridors.

In the end I would like to thank my family and Maša for their support and patience throughout my studies, especially during the (for everybody) difficult writing of my Ph.D. thesis.

Abstract

A novel soft-soft composite material, consisting of liquid crystal elastomer inclusions dispersed in a cured polymer matrix, is presented and studied. The so-called polymer-dispersed liquid crystal elastomer (PDLCE) [1] exhibits similar thermomechanical deformation as its liquid crystal elastomer (LCE) counterpart, i.e., a temperature driven mechanical reduction in length at the liquid crystal's nematic to isotropic phase transition. Unlike regular LCEs, which can be produced in limited amounts and shapes, the PDLCEs can be molded into arbitrary shapes and sizes, and, due to their practical synthesis procedure, implemented into already existing polymer and elastomer industrial processes. PDLCEs are prepared by freeze fracturing the LCE material into micro-sized particles and dispersing them into a polymer melt. By exploiting the anisotropic magnetic susceptibility of nematically ordered mesogen constituents, the LCE particles are aligned with a strong external magnetic field. The particle alignment is then locked by thermally curing the polymer matrix. The resulting PDLCE composite thermomechanically deforms by transferring the spontaneously induced strain of LCE particles onto the surrounding matrix. The degree of PDLCE deformation is governed by the relation between elastic constants of LCE material and polymer matrix, and the concentration of the LCE particles. Since LCE particles themselves act as inclusions, additional functionalization of PDLCEs can be achieved by further doping the polymer matrix or changing the species of LCE material. PDLCE with bimodal TM actuation is produced by using different LCE inclusions, something that cannot be achieved with regular LCEs. With an efficient milling process, the LCE particles can be reduced to monodomain sizes required for successful magnetic alignment, thus omitting the need for the unpractical two-step synthetization process to obtain monodomain LCE material, which involves a tedious step of aligning partially crosslinked LCEs with a mechanical load. A new synthesis process with magnetically driven alignment is proposed, which produces monodomain LCE particles completely equivalent to particles obtained with the two-step procedure. Therefore, the production of PDLCEs is not limited anymore by the tedious, low-yield synthesis of the initial LCE material, since it can be synthesized with ease and in virtually unlimited amounts. The degree of magnetic alignment of such particles is studied by deuterium perturbed ^{2}H-NMR spectroscopy and a model is derived to predict the obtained orientational order parameter. More complex thermomechanical deformations can be further achieved by combining different two layer combinations of functionalized and/or non-functionalized PDLCE material. Five basic morphing configurations are produced with this method that can act as voxels in 3D printing technology, a combination of which can be used to fabricate PDLCE material with arbitrary morphing abilities.

Povzetek

V moji disertaciji sta predstavljena razvoj in raziskava nove vrste termomehanskega mehko-mehkega kompozitnega materiala, poimenovanega polimerno dispergirani tekočekristalni elastomer (PDTKE). PDTKE se termomehansko deformira podobno kot TKE: dolžina vzorca se skrajša pri temperaturi nematsko/izotropnega faznega prehoda mezogenov, ki sestavljajo TKE delce, vsebovane v kompozitu. Glavna prednost PDTKE je njihova preprosta obdelava, saj se jih lahko oblikuje v poljubne oblike kakršnihkoli velikosti, kar naredi material primeren za prenos v že obstoječe polimerne in elastomerne industrijske postopke. PDTKE kompoziti so sestavljeni iz mikroskopsko velikih TKE delcev, dispergiranih v polimerni matriki. TKE delce pripravimo z zmrzovanjem in mletjem TKE materiala, ki ga umešamo v tekoči polimer. Z uporabo močnega magnetnega polja TKE delce nato uredimo v smeri polja s pomočjo magnetnega navora, ki nastane zaradi anizotropne diamagnetne susceptibilnosti nematsko urejenih mezogenov v TKE delcih. Nastalo urejenost nato zapišemo v kompozit s polimerizacijo zmesi pri višji temperaturi. Tako pripravljeni PDLCE kompoziti postanejo termomehansko odzivni, ker se nastale mehanske napetosti prenesejo preko sklopitve TKE delcev in okoliške matrike na celotni kompozit. Velikost deformacije je odvisna od razmerja med elastičnimi konstantami TKE in polimerne matrike ter od koncentracije vsebovanih TKE delcev. Ker TKE delci nastopajo kot vključki v kompozitu, je nadaljnja funkcionalizacija PDTKE mogoča že s preprostim dodajanjem različnega materiala v polimerno matriko ali z izbiro drugačnih vrst TKE delcev. Z uporabo dveh različnih vrst TKE vključkov je bil pripravljen PDTKE kompozit z dvostopenjskim termomehanskim odzivom, ki ga pri običajnih TKE-jih ni mogoče doseči. Z učinkovitim mletjem lahko TKE delce vedno zmanjšamo na enodomensko velikost, potrebno za uspešno magnetno urejanje, kar nam omogoča, da lahko opustimo zapleteno in nepraktično dvostopenjsko sintezo enodomenskega TKE, pri katerem je treba delno zamrežene TKE urejati s pomočjo mehanskih uteži. Z vpeljavo nove metode urejanja mezogenov z magnetnim poljem, s katero pripravimo delno urejeni TKE material, lahko proizvedemo enodomenske TKE delce, popolnoma ekvivalentne delcem, pridobljenim z dvostopenjsko sintezo. Na ta način proizvodnja PDTKE ni več omejena z dolgotrajnim sintetiziranjem majhnih količin LCE, saj z novo sintezno metodo lahko proizvedemo LCE material v praktično neomejenih količinah in brez zapletenih postopkov. Stopnja urejenosti teh delcev v kompozitu je bila izmerjena s tehniko ^{2}H-NMR spektroskopije, za katero je predstavljen tudi računski model za izračun orientacijskega parametra reda v kompozitu. Bolj kompleksne termomehanske deformacije lahko dosežemo s sestavljanjem različnih kombinacij funkcionaliziranega in/ali nefunkcionaliziranega PDTKE materiala v dvoslojne kompozite. Za demonstracijo je bilo pripravljenih pet osnovnih konfiguracij, ki bi lahko delovale kot voksli pri 3D tiskanju, katerih nadaljnje kombiniranje bi lahko uporabili za izdelovanje PDTKE materialov s poljubnimi deformacijskimi lastnostmi.

Contents

List of Figures **xv**

List of Tables **xvii**

Abbreviations **xix**

1 Introduction **1**

2 Liquid crystal elastomers **3**
2.1 Liquid crystals ... 3
2.2 Order parameter ... 4
2.3 Liquid crystal elastomers ... 5
2.4 Isotropic to nematic transition ... 6

3 Polymer dispersed liquid crystal elastomers **9**
3.1 Overview ... 9
3.2 PDLCE composites ... 9
3.3 Orientational order parameter of μLCEs ... 10
3.4 Magnetic alignment of μLCEs ... 12

4 Nuclear magnetic resonance **17**
4.1 Nuclear spin Hamiltonian ... 17
4.2 Quadrupole interaction ... 18
4.3 ^{2}H-NMR of liquid crystals ... 20

5 Experimental methods **23**
5.1 LCE preparation ... 23
5.2 PDLCE preparation ... 25
5.3 Thermomechanical and stress-strain measurements ... 26
5.4 ^{2}H-NMR measurements ... 27
5.5 List of LCE samples ... 27

6 PDLCE characterization and optimization **29**
6.1 Thermomechanical response of PDLCE species ... 29
6.2 Investigation of PDLCE's structure ... 32
6.3 Modeling of PDLCE's elastic and thermomechanical properties ... 33
6.4 Optimization of PDLCE properties ... 36
6.5 Effect of setting temperature on the PDLCE response ... 38

7 ^{2}H-NMR spectroscopy of PDLCE composites **41**
7.1 Modeling the ^{2}H-NMR spectra ... 41
7.2 Sample preparation ... 44

7.3 Impact of viscosity on μLCE alignment 44
7.4 Determining the orientational order parameter Q 49

8 PDLCE bilayer composites **53**
8.1 Morphing of PDLCE discs 53
8.2 Basic morphing configurations using PDLCE bilayers 53
8.3 PDLCE actuator 56
8.4 PLDCE bilayer preparation 57

9 Conclusions **59**

References **63**

Bibliography **67**

Biography **69**

List of Figures

Figure 2.1: Typical phases found in liquid crystal systems. 3
Figure 2.2: Orientation of molecules with respect to director $\mathbf{n}$. 4
Figure 2.3: Main chain and side chain liquid crystal elastomer. 5
Figure 2.4: Polydomain and monodomain LCE. 6
Figure 2.5: Evolution of the order parameter at different field strengths. 8
Figure 3.1: PDLCE preparation scheme. 10
Figure 3.2: Preparation of LCE microparticles. 11
Figure 3.3: Order parameter Q and alignment time τ_0 15
Figure 4.1: Energy levels of a spin 1 nucleus. 20
Figure 4.2: Deuterated mesogen M(D)6 and its orientation in the magnetic field. 21
Figure 5.1: Compounds used in the synthesis of LCE systems: 23
Figure 5.2: Director alignment using a mechanical load. 24
Figure 5.3: PDLCE preparation sequence. 25
Figure 5.4: Experimental setup 26
Figure 6.1: Thermomechanical responses of various PDLCE species. 30
Figure 6.2: Two-step PDLCE composite. 31
Figure 6.3: PDLCE structure under a polarizing optical microscope. 32
Figure 6.4: Layer geometry for the series and parallel model. 34
Figure 6.5: Optimization of PDLCE properties. 37
Figure 6.6: PDLCE performance. 39
Figure 7.1: PDLCE sample position inside the RF coil. 44
Figure 7.2: Calculated time-dependent viscosity of PDLCE polymer matrix. 45
Figure 7.3: Evolution of order parameter Q during the alignment process. 47
Figure 7.4: Estimated order parameter at different magnetic fields. 48
Figure 7.5: Recorded and simulated spectra of PDLCE-Ds. 49
Figure 7.6: Derived orientational distribution σ_θ with associated second moment M_2 . . 50
Figure 7.7: Determination of order parameter $Q(\sigma_\theta)$. 51
Figure 8.1: TM deformation of disk shaped PDLCEs. 54
Figure 8.2: Bilayer PDLCE's morphing configurations. 55
Figure 8.3: PDLCE bilayer actuator. 57

List of Tables

Table 5-1: List of LCE materials used for PDLCE preparation. 28
Table 6-1: List of all PDLCE samples. 29

Abbreviations

LCE	... Liquid crystal elastomer
PDLCE	... Polymer-dispersed liquid crystal elastomer
LC	... Liquid crystal
LdG	... Landau-de Genes
I-N	... Isotropic to nematic transition
PN-N	... Paranematic to nematic transition
μLCE	... Liquid crystal elastomer microparticles
NMR	... Nuclear magnetic resonance
RF	... Radiofrequency
^{2}H-NMR	... Deuterium nuclear magnetic resonance
EFG	... Electric field gradient
M4	... 4-methoxyphenyl 4-(but-3-en-1-yloxy) benzoate
M11	... 4-methoxyphenyl 4-(undec-10-en-1-yloxy) benzoate
V1	... 1,4-bis (undec-10-en-1-yloxy) benzene
M(D)6	... Deuterated 4-methoxyphenyl 4-(hex-5-en-1-yloxy) benzoate
TM	... Thermomechanical
PDMS	... Polydimethylsiloxane

Chapter 1

Introduction

The widespread use of polymers and elastomers in modern technology is not only attributed to their versatile mechanical properties, but also relies on the fact that they are relatively undemanding for molding, reshaping and machining with non-complicated manufacturing processes. Polymer and elastomer parts are in most applications used as passive mechanical elements. But to enhance their functionality, they could be replaced by recently developed smart materials that have a mechanical responsiveness to different external stimuli, for instance to an electric field [2], that are already being employed for use in the actuation industry. One of these smart soft materials are liquid crystal elastomers (LCEs) [3] that are also becoming increasingly strong competitors in this area.

LCEs are materials that combine elastic properties of polymeric networks with orientational properties of mesomorphic molecules. This gives them the ability to reversibly change its shape, a consequence of a temperature-driven reversible transition from an ordered to disordered state of liquid crystal molecules situated within the LCE. The development of LCEs for their use as actuators and transducer elements is currently focused on macroscopic devices, e.g. artificial muscles [4] and micro- and nano-sized devices, such as MEMS and NEMS [5]. Aside from this, they have already been used in many prototype devices [6], while new scientific achievements are widening their applicative potential [7], [8]. Nevertheless, there are some setbacks that prevent LCEs direct applicative integration, one of them being their size and shape limitations. Because of complex synthetization methods, macroscopically sized LCEs are limited mostly to thin films [9], while synthesis of different geometrical shapes can only be achieved at small yields and at nano- to micro-dimensions [10].

To overcome these problems, polymer-dispersed liquid crystal elastomers (PDLCEs) are introduced here as a new thermomechanically functional composite material which can be molded into any arbitrary shape and size. PDLCEs are prepared by freeze-fracturing regular LCEs into microparticles and dispersing them into a curable polymer mixture. This mixture is cured in an external magnetic field, which aligns the particles along the field direction. Simultaneously, particles' orientational order is quenched by curing the resin. With this method the thermomechanical deformation of the LCE particles is transferred onto the polymer matrix, granting the bulk composite the ability to deform in the same manner.

Because the PDLCE pre-polymer mixture is in a paste form, it can be simply injected and further molded into any shape and size, as well as applied to manufacturing processes that have already been developed for regular elastomers or polymers. While spatially modulated ordering of LCEs to achieve different shape change is possible ([8], [11]), shape-programming on a larger scale can be realized only by cutting and combining different LCE layers together. PDLCE material, on the other hand, can be applied to additive

manufacturing techniques to achieve the same by deposition and progressive ordering of layers with an external field, making the process much simpler and faster. This makes PDLCEs ideal for integration into newly emerging and popular 3D-printing technology. Different morphing abilities are therefore implemented by modulating the nematic director throughout the PDLCEs volume, making the PDLCE material itself the carrier of the shape-changing properties. This means that there is also no need for inhomogeneous or local fields to achieve shape-changes of higher complexity as is the case for uniformly oriented LCEs [12].

It is also possible to custom tune thermomechanical properties by simply changing LCE concentrations and/or by using LCEs with different thermomechanical characteristics. PDLCEs have the advantage of being further functionalizable by using different dopants dispersed into the polymer network. Since LCEs in PDLCEs act as inclusions, the LCEs themselves do not need to carry additional properties for further functionalization of the composite material, so additional functionalization of the LCE material and pertaining difficulties arising from their synthetization method ([10], [11]) can now be avoided. This opens many new ways of producing elastomers with custom properties that can satisfy diverse industrial needs and also providing for a new generation of scientifically intriguing soft-soft systems.

The scope of this doctoral thesis is a detailed description of preparation of PDLCE composites and their characterization and optimization. By changing the concentration of LCE particles and Young's modulus of the polymer matrix, one is able to determine the influence of these parameters on the degree of thermomechanical response and overall PDLCE elastic constant. ^{2}H-NMR spectroscopy can be used to determine how the magnetic field affects the orientational order of LCE particles inside the PDLCE composite. For this purpose, LCEs containing deuterated M(D)6 mesogen molecules were synthesized, from which PDLCE composites were produced under different magnetic fields. Deuterated mesogens enable one to record the quadrupole-perturbed deuterated NMR spectra. The obtained results were analyzed by comparing measurements to simulations of spectra within the chemical exchange model of the nematic director and deriving the desired parameters. To show the concept of additional functionalization of PDLCEs, a two-step composite was made, containing particles from two LCE species with different transition temperatures. The resulting composite exhibits two sequential deformations with increasing temperature. Differently functionalized and non-functionalized PDLCE materials were combined into simple bilayers to achieve different shape changes in order to demonstrate how one can utilize the PDLCE material for 3D-printing technology. These shapes can also act as basic voxels, the combination of which can produce customized morphing PDLCEs with arbitrary reversible shape change. A bilayer actuator was also prepared in the same manner, exhibiting a trigger-like deformation which only takes place within a certain temperature interval.

Chapter 2

Liquid Crystal Elastomers

2.1 Liquid Crystals

Liquid crystals (LCs) are molecules that exhibit a state of order between crystalline lattices and isotropic fluids. They flow like fluids while they also exhibit ordering in a similar way as in a crystal. This intermediate state is called a 'mesophase'. The phases that LCs exhibit are distinguished among themselves by the orientational order of the molecules. This order is governed by the anisotropic shape of the LC molecules, by which the molecules are encouraged to be parallel to each other due to steric effects. The shape exclusion is larger at higher concentrations and LCs which exhibit concentration-dependent ordering are called lyotropic LCs. Another ordering mechanism comes from the short-range potential forces between the molecules. These are related to the van der Waals interaction between the molecules that are the strongest when the LC molecules are parallel. Higher ordering is achieved at lower temperatures while at higher temperatures thermal fluctuations destroy the order. LCs whose phase transitions are influenced by temperature are called thermotropic LCs [13], [14].

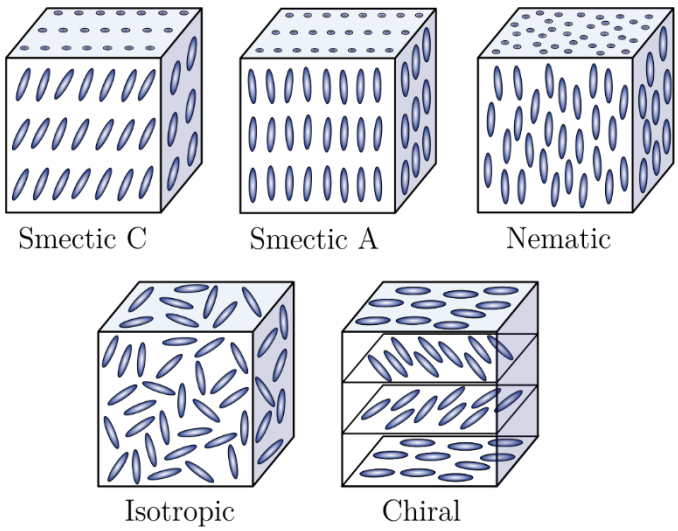


Figure 2.1: Typical phases found in liquid crystal systems. Depicted are the higher ordered smectic C and smectic A phase, with characteristic orientational and lateral LC ordering, the nematic phase exhibiting only orientational molecular ordering and the isotropic phase, where the molecules are randomly oriented throughout the system. LCs can also form a chiral phase, consisting of nematically ordered, helically twisted molecular planes.

When dealing with rod-like LC molecules, the basic mesophases that exist between the liquid isotropic phase and completely solid crystal phase are the nematic, smectic and chiral phases (Figure 2.1) [13]–[15]. In the nematic phase, LC molecules exhibit average orientational ordering of long molecular axes in one particular direction but are randomly distributed throughout the system. Molecules in the smectic phase possess the same orientational ordering, but also show additional translational ordering which results in a layered formation. The smectic phase can be further characterized into smectic A or smectic C phase, depending on the tilt of molecular orientation as shown in Figure 2.1. The chiral phase is a special form of a nematic phase that has a helical twist about an axis perpendicular to the long molecular axis.

2.2 Order Parameter

What state or phase the system is in is described by the order parameter S. In LC systems with rod-like molecules, the direction of nematic ordering is described by the nematic director $\mathbf{n}$, which is a unit vector that only shows the principal axis of alignment. It is a double headed vector since the direction along ordered rods is symmetrical in both directions. The degree of molecular orientation is described by the nematic order parameter S_N, defined via the average of second Legendre polynomial as [13], [15]

$$S_N = \left\langle P_2(\cos\theta) \right\rangle = \left\langle \tfrac{3}{2}\cos^2\theta - \tfrac{1}{2} \right\rangle \tag{2.1}$$

where θ is the angle between the nematic director $\mathbf{n}$ and molecular orientation (Figure 2.2), with the brackets $\langle ... \rangle$ denoting the average over molecular directions θ. When $S_N = 1$, LCs exhibit a perfect nematic order where all molecules are directed up $(\theta = 0)$ or down $(\theta = \pi)$. For $S_N = 0$, molecules are randomly oriented, the phase is isotropic and $\langle \cos^2\theta \rangle = 1/3$ [13]. In reality $S_N = 1$ can never be reached and the value of S_N is always below 1, but a negative value can be reached down to $S_N = -1/2$, when the molecules are perpendicular to the nematic director $\mathbf{n}$.

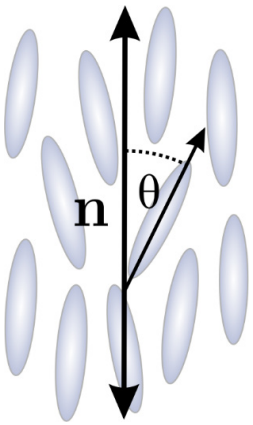


Figure 2.2: Orientation of molecules with respect to director $\mathbf{n}$. The nematic order parameter S_N is determined by the average tilt of molecular long axis against the nematic director $\mathbf{n}$, denoted by angle θ.

2.3 Liquid Crystal Elastomers

Liquid crystal elastomers are networks of crosslinked polymer chains with attached mesogenic molecules. This structure combines intrinsic liquid crystalline ordering with elastic properties of the polymer network, giving LCEs the ability to deform its shape with changing temperature. The mesogen molecules can be attached to the polymer chain in two ways: they can be either linked together in a head-to-tail fashion to form a main chain elastomer (Figure 2.3 (a)) or attached via a flexible backbone, resulting in a comb-like topology, forming a side chain elastomer (Figure 2.3 (b)) [13].

The average shape of the polymer network is normally spherical. For nematic elastomers, both for main and side chain elastomers, the polymer backbone average shape is distorted by the nematic order of the mesogen molecules. When the nematic order is high, the whole polymer network is forced into a directed shape and the average shape elongates. In the isotropic phase, the elastomer's average shape is again spherical.

This property gives LCEs the ability to deform, i.e., contract in length while going from nematic to isotropic transition with increasing temperature and returning to its original size when the temperature decreases. For nematic side-chain LCEs, this reduction in length is typically about $40\% - 50\%$ of its initial size. For an LCE to reach a high degree of deformation, it is important that it consists of a single nematic domain (monodomain LCE), i.e., that the nematic director of mesogenic molecules is oriented in the same direction uniformly along the LCE length. If the LCE is a polydomain, it consists of many domains of locally oriented nematic directors. Because the domain directors are randomly oriented across the LCE, the linear contraction of such LCEs does not occur, since the effect is averaged out.

A way to produce a well-ordered LCE structure is by applying an external field to additionally orient the nematic directors along the field direction. Nematic LCs have anisotropic dielectric and diamagnetic susceptibilities, so it is possible to align them by means of an electric or magnetic field, unless the anchoring at their boundaries is too strong. Such is the case when LCEs are fully polymerized where anchoring, resulting from mechanical constraints of cross-linked polymer network, prevents successful alignment of nematic directors. One way of producing ordered LCEs is to use a large enough electric or magnetic external field during the synthesis in order to reach a nematic state in the LCE

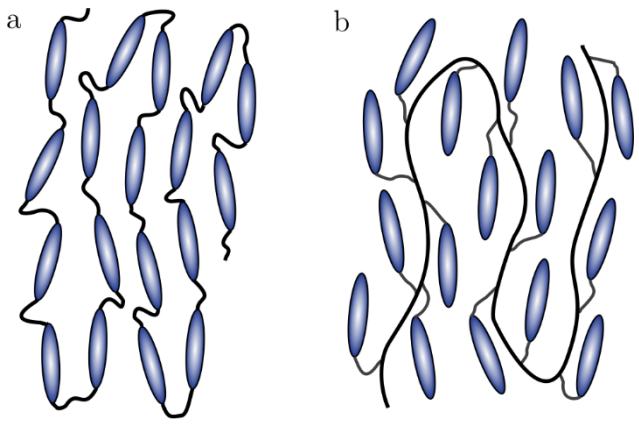


Figure 2.3: Main chain and side chain liquid crystal elastomer. Main chain elastomers are composed of mesogenic monomers, linked together at both ends to form a polymeric chain (a), while in side chain elastomers, the mesogens are at one side attached to the polymeric chain via a flexible backbone (b).

melt before the polymer network is formed. After cross-linking, the alignment is anchored to the polymer network and preserved by the formed structure [13], [16].

Another way of establishing orientational order is by using a mechanical field in a two-step synthesis process, pioneered by Finkelmann et al. [9]. At first, the LCE melt is partially cross-linked and swollen to form a gel. It is then stretched so that the mechanical field acting upon the polymeric network induces the orientational alignment of mesogens along the field direction. The induced ordered structure is then frozen in the second step by further cross-linking the sample, preferably at temperatures below the nematic-isotropic phase transition. If the above procedure is performed at higher temperatures, when the LCE is in the isotropic phase, a larger mechanical load must be applied to hold the elastomer in the nematic state. In both cases, the use of a large enough mechanical field will result in a monodomain LCE [9], [13].

Successful alignment can be quickly confirmed by checking the transparency of the LCE sample. The polydomain LCE will be opaque because of the strong light scattering on the randomly oriented nematic domains, whereas monodomain LCEs will be completely transparent [9], [13]. This is in contrast to nematic LCs, which are turbid due to thermal director fluctuations. Nematic monodomain LCEs do not scatter light since the thermal excitation energy penalty is too high to induce director rotations, as a result of strong mesogen anchoring.

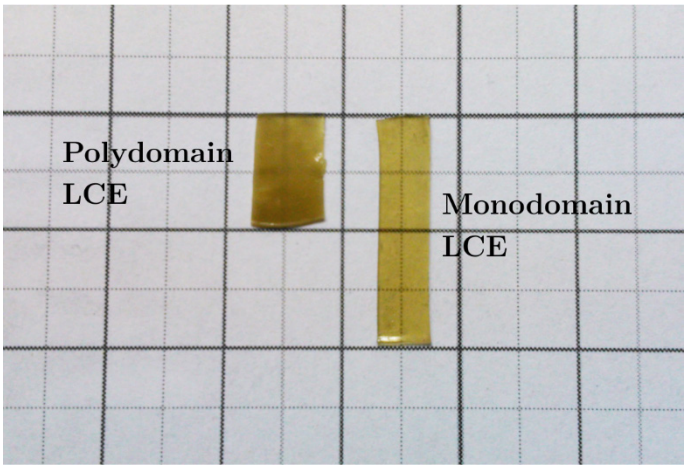


Figure 2.4: Polydomain and monodomain LCE. When the alignment procedure is omitted, the LCE structure consists of multiple domains with randomly oriented nematic directors. Such LCEs are termed polydomain and are characterized by their opaque appearance. If the LCE's nematic director is well-aligned, the LCE becomes transparent and is considered to be monodomain.

2.4 Isotropic to Nematic Transition

Phase transitions can in general be characterized by observing the behavior of thermodynamic potentials and their derivatives. The potential derivatives provide information on the nature of phase transition being either of the first or second order. The first-order transition occurs when the first derivative of thermodynamic potentials exhibits a jump at the transition point. This means that the transition is abrupt and involves a nonzero latent heat. If the first derivative is continuous and the second converges at the

transition, it is considered a second-order transition, where the transition itself changes gradually and no latent heat is involved [15].

To describe the orientational and translational order during phase transitions one has to employ a mean-field Landau-de Genes (LdG) approach. In LdG theory, free energy F is expanded near the vicinity of the transition in respect to the order parameter and minima of the free energy are calculated for the desired parameter (pressure, temperature etc.) [15]. For nematic LCs, the free energy expansion reads [6], [13], [15]

$$F_N = \frac{1}{2} A S_N^{\,2} + \frac{1}{3} B S_N^{\,3} + \frac{1}{4} C S_N^{\,4}. \tag{2.2}$$

A, B and C are the Landau expansion coefficients and S_N is the nematic order parameter. Coefficient A is temperature-dependent and takes a linear form: $A(T) = a(T - T^*)$. Here, temperature T^* marks the absolute metastability limit of the isotropic phase. Other coefficients, a , B and C, are considered to be temperature independent. Thermodynamic equilibrium is achieved at the minimum of F_N. Derived solutions of $\partial F_N / \partial S_N = 0$ are:

$$\begin{aligned} S_I &= 0, \\ S_N &= \frac{B}{4C}\left[1 + \sqrt{1 - \frac{24a(T - T^*)\mathrm{C}}{B^2}}\right] > 0, \\ S_3 &= \frac{B}{4C}\left[1 - \sqrt{1 - \frac{24a(T - T^*)\mathrm{C}}{B^2}}\right]. \end{aligned} \tag{2.3}$$

The first solution S_I signifies the order parameter in the isotropic phase, while the second, S_N, in the nematic phase. Solution S_3 should be disregarded since this state cannot be achieved in equilibrium. The derived temperature-dependent order parameter exhibits a discontinuity at the isotropic-nematic (I-N) transition temperature, which is calculated to be [6], [13], [15]

$$T_{I-N} = T^* + (2B^2/9aC). \tag{2.4}$$

If an external field is present in the system, as is the case when an electrical or magnetic field is applied onto LCs or a mechanical field onto LCEs, the free energy expansion contains an additional linear term $-GS_N$, which represents the effect of the external field [6], [17]:

$$F_N = \frac{1}{2} a(T - T^*) S_N^{\,2} + \frac{1}{3} B S_N^{\,3} + \frac{1}{4} C S_N^{\,4} - G S_N \ . \tag{2.5}$$

An applied external field can induce orientational order even in the isotropic phase and can eliminate the discontinuity of the N-I transition so that it becomes of the second order. This intermediate phase is called a paranematic phase. The discontinuity depends on the

value of the applied field G (Figure 2.5 – graph taken from [18]), which has a critical value at

$$G_C = -B^3 / 27C^2 . \tag{2.6}$$

The transition remains first-order if $G < G_C$. The discontinuity vanishes when the field reaches $G = G_C$ and at higher values, $G > G_C$, a 'supercritical' regime is reached and the transition becomes second-order. The transition temperature, now from the paranematic to nematic phase (PN-N), is also shifted by the additional field and becomes:

$$T_{PN-N} = T^* + \frac{2B^2}{9aC} + \frac{3CG}{aB} \quad . \tag{2.7}$$

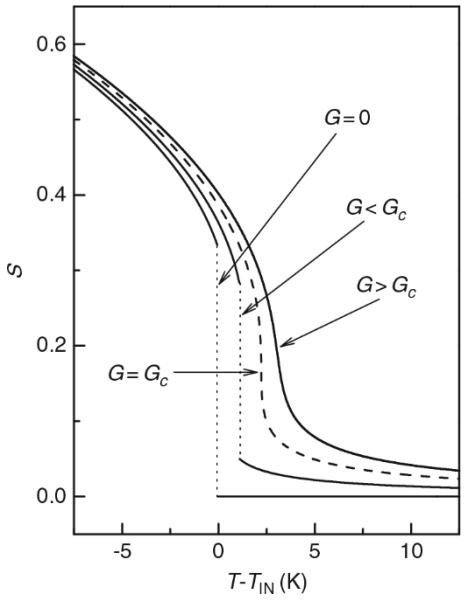


Figure 2.5: Evolution of the order parameter at different field strengths. In zero field ($G = 0$), the order parameter exhibits a discontinuous jump at the phase transition temperature. This is defined as a first-order phase transition. When the field is increased ($G \to G_C$), the discontinuity begins to evolve into a continuous transition and for $G > G_C$, the order parameter exhibits a wide and steady transition between phases, deemed as a second-order phase transition.

Chapter 3

Polymer-Dispersed Liquid Crystal Elastomers

3.1 Overview

LCEs have an outstanding potential to be used in actuation technologies, but as already discussed, their size and shape limitations (among other), are preventing successful implementation into larger scale production environment. To elaborate further, one of the major obstacles is found in the microscopic size of LCE domains. Current polymerization methods can only yield isotropic distribution of domain orientations, which in consequence hinders overall LCE deformation. For now the most efficient way of instilling domain orientation is to apply mechanical stress to partially crosslinked LCE network [9] (see Section 2.3). It is found that this orientation procedure is not practical and must be performed manually, since it involves careful handling and practice. Even if this procedure was automated, only thin strip-form samples with unidirectional shape deformation could be made. However, patterned domain orientation can be achieved by means of photoalignment [8], [19], but this technique can be applied only on thin films and still includes partial crosslinking of the specimen. And while a new, recently invented method [7] omits partial crosslinking, the domain orientation again has to be performed mechanically.

A completely moldable LCE material without any shape and size limitations, and with a potential to be applied to current elastomer production processes or additive manufacturing has yet to be developed. In this thesis, a new composite material called polymer-dispersed liquid crystal elastomers (PDLCEs) is presented, which can overcome the aforementioned restrictions.

3.2 PDLCE Composites

The main idea behind PDLCEs is to dope the conventional silicone elastomer with LCE microparticles (μLCE) to functionalize the composite material with thermomechanical properties, giving it the ability to shape-change in a similar manner as an LCE material. To successfully render the composite thermomechanically active, the μLCE must be aligned, i.e. their nematic directors must face the same general direction, equivalent to domains in LCEs, otherwise the PDLCE stays inert. This can be achieved by exploiting LC's anisotropic magnetic susceptibility [20], thus aligning μLCEs with a magnetic field. The magnetic field applied on the polymer-μLCE mixture produces a large enough torque on μLCE particles to align them in the field direction. The induced anisotropic order is

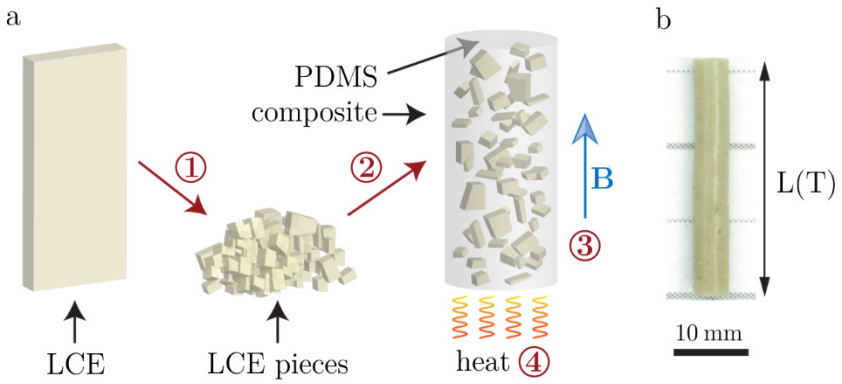


Figure 3.1: PDLCE preparation scheme. (a) LCE strips are first crushed into μLCEs (1), which are then mixed into the PDMS matrix (2). A magnetic field is applied to the PDMS/LCE mixture to orient the μLCEs along the field direction (3). When oriented, the mixture is heat-cured to lock the particles in place (4). (b) The resulting PDLCE samples were cylindrically-shaped for experimental purposes.

then incorporated into the PDLCE by curing the surrounding polymer matrix with heat or UV-radiation.

The prerequisite for the magnetic alignment to take place is that μLCEs have a well-defined nematic order. Numerous techniques for producing monodomain μLCE particles have been introduced recently, as for example templating [21], [22], using a microfluidic approach [23] or using a 3D direct laser writing technique [24], yet the yield is not large enough nor the production fast enough for producing bulk macroscopically sized PDLCE composites. To resolve this, a monodomain LCE can be freeze-fractured into micropowder. This way one can obtain arbitrary amounts of small enough particles to be used as inclusions and, most importantly, the μLCEs themselves still retain their monodomain nature. While monodomain LCEs are the best option to obtain highly ordered μLCE particles, one can also use polydomain LCEs and crush them down to their single domain size, which for polydomain LCEs is typically around several μm [13]. One can now bypass any complicated synthesis procedure for obtaining monodomain LCEs and make use of polydomain LCE material that can be produced in unlimited amounts.

With an efficient fracturing technique to obtain small enough μLCE particles, then mixing them into a polymer matrix and aligning them under a magnetic field, one can produce a PDLCE composite. Since the μLCE surfaces are completely adhered to the surrounding matrix, mechanical stresses from μLCEs, induced by thermomechanical deformation, are transferred onto the whole composite and the PDLCE is deformed in a similar manner as a regular LCE. Because no mechanical aligning process is needed to obtain nematic ordering, PDLCEs can be produced in any arbitrary shape or size. Further functionalization of PDLCEs can also be obtained by simply dispersing additional material into the polymer matrix and thus avoiding difficulties imposed by the complicated doping of LCEs [25], [26]. The surrounding matrix could then exhibit additional improved properties, such as enhanced thermal or electrical conductivity [27], [28].

3.3 Orientational Order Parameter of μLCEs

As μLCEs retain the nematic alignment of LCEs from which they are made of, the same nematic director $\mathbf{n}$ can be applied to each individual μLCE particle. One can say that $\mathbf{n}$

is static within the µLCE and is pointing in the direction of the average alignment of particle's nematic order when dealing with multi-domain LCE particles. When µLCEs are dispersed into a polymer melt, their nematic directors are randomly oriented. Their nematic director distribution, $P(\cos\vartheta)$, is therefore isotropic,

$$P_0(\cos\vartheta) = \frac{1}{2}. \tag{3.1}$$

When µLCEs are aligned in an external applied magnetic field, the anisotropy increases,

$$P_t(\cos\vartheta) = \int_0^1 \delta\left[\cos\vartheta - \cos\vartheta(t,\cos\vartheta_0)\right] \mathrm{d}\cos\vartheta_0 . \tag{3.2}$$

Here, t is the time from the start of the director alignment and δ denotes the Dirac Delta function. The term $\cos\vartheta(t,\cos\vartheta_0)$ describes the alignment of a µLCE's nematic director, which has its initial orientation at $\vartheta_0 \angle(\mathbf{n},\mathbf{B})$ at time $t = 0$. This term is obtained by solving the equation of motion for the given µLCE particle. During alignment, the distribution $P_t(\cos\vartheta)$ possesses cylindrical symmetry (independent of azimuthal angle φ) about $\mathbf{B}$ and is invariant to the transformation $\vartheta \to \pi - \vartheta$.

As seen in Section 2.2, the orientational order of nematic director is quantified by the order parameter $S_N = \left\langle \frac{3}{2}\cos^2\theta - \frac{1}{2} \right\rangle$ (note that θ describes the angle between long

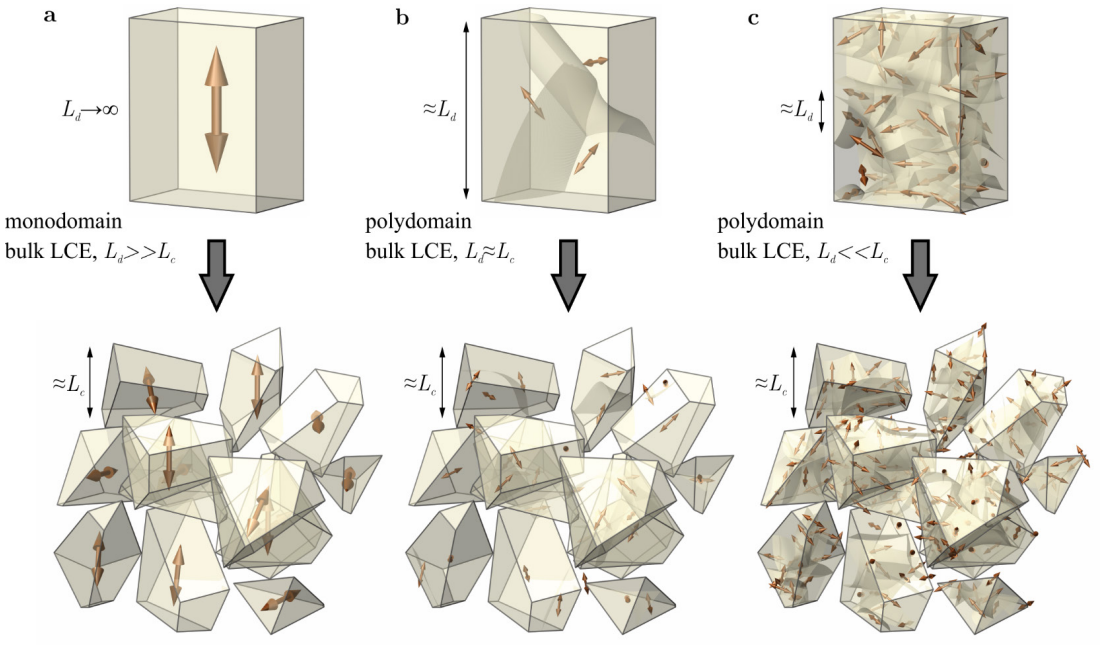


Figure 3.2: Preparation of LCE microparticles. (a) After crushing monodomain LCEs, the resulting µLCE retain the monodomain nature, since the particle diameter L_c is smaller than the average domain size L_d. When $L_d \approx L_c$ (b), the particles consist of multiple domains, but nevertheless some nematic order is still preserved and particle reorientation is still possible. Only when LCE domain sizes are smaller than µLCEs, $L_d << L_c$, the particles are considered isotropic with no definite nematic director. A successful magnetic alignment of such particles cannot be achieved.

molecular axis and nematic director), in which the average is performed over the distribution $P(\cos\theta)$. In case of PDLCEs a global orientational order parameter Q is introduced, which in this case describes the μLCE's orientational order in a given PDLCE. Taking into account Equation (3.2), it takes the form:

$$Q(t) = \frac{1}{2}\int_0^1 (3\cos^2 \vartheta(t, \cos\vartheta_0) - 1)\, \mathrm{d}\cos\vartheta_0 \,. \tag{3.3}$$

In PDLCEs, prepared in an external magnetic field $\mathbf{B}$, with order parameter $Q \approx 1$, the incorporated μLCE particles are well aligned. A high order can only be achieved with particles possessing a well-defined nematic order, i.e. consisting of a single nematic domain. When particles have multiple domains or the orientational order was quenched before the alignment process was complete, the Q values lie in the range $0 < Q < 1$. If PDLCE is cured without an applied magnetic field, no alignment of μLCE particles occurs, so they remain isotropically oriented ($Q = 0$) and the PDLCE is considered isotropic. Without μLCE orientational order, isotropic PDLCEs are inert in terms of thermomechanical response, while specimens having $Q > 0$ exhibit observable shape change in the alignment direction.

Caution must be taken not to mistake Q, which describes the orientational order of μLCEs, for order parameter S_N, which measures the nematic order of LC molecules, imprinted inside the microparticle domains. Q is therefore also independent of temperature, since the orientational distribution is fixed upon PDLCE's polymerization. S_N, on the other hand, is strongly dependent on temperature as already described in Section (2.4), with the phase transitions manifesting themselves in PDLCE's thermomechanical response.

3.4 Magnetic Alignment of μLCEs

LCE microparticles can be described as spherical particles, each with its own nematic director. A torque is induced upon the particles by the magnetic field due to the diamagnetic susceptibility of mesogenic molecules. Magnetic torque is described by

$$\Gamma_B = -\frac{1}{2} V \chi_a \mu_0 H^2 \sin 2\vartheta \,, \tag{3.4}$$

where V is the μLCE volume, χ_a magnetic susceptibility anisotropy, μ_0 magnetic constant or vacuum permeability and H the magnetic field strength. ϑ is the angle between the magnetic field and the nematic director of the μLCE particle.

Since LCs are diamagnetically anisotropic, the magnetic susceptibility anisotropy χ_a can be determined from the two principal values, $\chi_{||}$ and $\chi_{\perp}$, where $||$ signifies the parallel and $\perp$ the perpendicular component. It is also associated with the nematic order parameter S_N by [29]:

$$\chi_a = (\chi_{||} - \chi_{\perp}) S_N = \Delta\chi S_N \,. \tag{3.5}$$

By considering that $H = \mathrm{B}/\mu_0$ and using trigonometric identity $\sin 2\vartheta = 2\sin\vartheta\cos\vartheta$, the magnetic torque can be written as:

$$\Gamma_B = -\frac{1}{\mu_0} V S_N \Delta\chi B^2 \sin\vartheta \cos\vartheta \,. \tag{3.6}$$

μLCEs are dispersed in an uncured matrix, so in addition to magnetic torque they also experience a viscous torque

$$\Gamma_\eta = -8\pi\eta r^3 \frac{d\vartheta}{dt}, \tag{3.7}$$

with η denoting viscosity of the polymer melt and r the effective particle radius. Here, the viscous torque is written for a sphere-like particle. If the particle is approximated with an ellipsoid, a geometrical factor $F(r/R)$ [30] must be included to yield:

$$\Gamma_\eta = -\frac{8\pi\eta r^3}{F(r/R)} \frac{d\vartheta}{dt} \,. \tag{3.8}$$

r and R are the radii of the short and long axis of the ellipsoid, respectively. For a sphere, $(r/R = 1)$, factor $F(r/R)$ equals 1 and for a moderately deformed sphere, its value is slightly decreased, e.g. $F(0.5) \approx 0.9$, $F(2) \approx 0.7$ [30]. Because μLCEs are more similar to spheres than rods or disks, one can approximate $r \approx R \Rightarrow F \approx 1$.

The equation of motion can now be calculated. The sum of torques acting on a LCE microparticle reads

$$I \frac{d^2\vartheta}{dt^2} = \Gamma_B + \Gamma_\eta \,. \tag{3.9}$$

The moment of inertia for a sphere is $I = 2\rho V R^2/5$, with ρ being the density of the particle. Inserting the moment of inertia and both the viscous and magnetic torque into Equation (3.9) one gets

$$\frac{2}{5}\rho V R^2 \frac{d^2\vartheta}{dt^2} = -\frac{1}{\mu_0} V S_N \Delta\chi B^2 \sin\vartheta\cos\vartheta - \frac{8\pi\eta r^3}{F(r/R)} \frac{d\vartheta}{dt}, \tag{3.10}$$

which can be further simplified using $V = 4/3\pi r^3$ and $F(\mathrm{r/R}) \approx 1$, into

$$\frac{2}{5}\frac{\mu_0 \rho R^2}{S\Delta\chi B^2} \frac{d^2\vartheta}{dt^2} = -\sin\vartheta\cos\vartheta - \frac{6\eta\mu_0}{S\Delta\chi B^2} \frac{d\vartheta}{dt}. \tag{3.11}$$

By defining two characteristic times,

$$\tau = \frac{6\eta\mu_0}{S\Delta\chi B^2} \tag{3.12}$$

and

$$\tau_R = \frac{\rho R^2}{15\eta}, \tag{3.13}$$

Equation (3.11) can be rewritten,

$$\tau\tau_R \frac{d^2\vartheta}{dt^2} = -\sin\vartheta\cos\vartheta - \tau\frac{d\vartheta}{dt}. \tag{3.14}$$

The characteristic time τ describes the alignment time, while τ_R is a timescale associated with the μLCE's radius. To further describe the impact of μLCE's radius R, it is best to introduce a dimensionless time $\tilde{t} = \mathrm{t}/\tau$ and a dimensionless particle acceleration term, $\alpha = \tau_\mathrm{R}/\tau = \mathrm{R}^2/\mathrm{R}_0^2$, with a newly defined characteristic radius

$$R_0 = \frac{3\eta}{B}\sqrt{\frac{10\mu_0}{\rho S \Delta\chi}}, \tag{3.15}$$

which determines the magnitude of the particle reorientational acceleration. Using these newly defined terms, Equation (3.14) rewrites into

$$\alpha\frac{d^2\vartheta}{d\tilde{t}^2} = -\sin\vartheta\cos\vartheta - \frac{d\vartheta}{d\tilde{t}}. \tag{3.16}$$

For $\alpha \ll 1$, which is satisfied for $R_0 \gg R$, the left acceleration part in the equation of motion is small enough to be considered zero. An estimation for α can be made with PDLCE's material specifics: $\eta \approx 3.5\,\mathrm{Pas}$ for PDMS, $\rho \approx 10^3\,\mathrm{kgm}^{-3}$, $S(T_{room}) \approx 0.8$ and $\Delta\chi \approx 10^{-7}$ [29] for M4 mesogens. In magnetic fields of $B \leq 9$, the characteristic radius is $R_0 \geq 0.5\,\mathrm{m}$, and considering that μLCE particle size ranges below $100\,\mu\mathrm{m}$, α becomes small enough to disregard the left acceleration term in Equation (3.16). The μLCE's reorientational dynamics can now be written as [31]

$$\frac{d\vartheta}{d\tilde{t}} = -\sin\vartheta\cos\vartheta. \tag{3.17}$$

We set the initial conditions at the moment when magnetic field B is turned on by requiring that microparticles are still $(d\vartheta/d\tilde{t}(\tilde{t}=0)=0)$, so the μLCE's starting orientation is determined by ϑ_0, $\vartheta(\tilde{t}=0)=\vartheta_0$. Assuming that $\Delta\chi > 0 \Rightarrow \tilde{t}(t>0) > 0$, the solution is derived by accordingly integrating Equation (3.17), which results in

$$\cos\vartheta(\tilde{t}, \cos\vartheta_0) = \frac{1}{\sqrt{1 + \frac{1-\cos^2\vartheta_0}{\cos^2\vartheta_0}e^{-2\tilde{t}}}}. \tag{3.18}$$

Solving the equation of motion, the orientational order parameter Q (see Equation (3.3)) can now be calculated:

$$Q(\tilde{t}) = \frac{\sqrt{e^{2\tilde{t}}-1}\left(1+2e^{2\tilde{t}}\right) - 3e^{2\tilde{t}}\arctan\sqrt{e^{2\tilde{t}}-1}}{2\left(e^{2\tilde{t}}-1\right)^{3/2}}. \tag{3.19}$$

By analyzing Equation (3.19) (see also Figure 3.3), one can see that the resulting $Q(\tilde{t})$ monotonously increases from the isotropic value at $Q(\tilde{t}=0)=0$ until saturating at

$Q(\tilde{t} \to \infty) = 1$ for $t \gg \tau$, signifying complete alignment of LCE microparticles. An estimation of the alignment timescale can now be made (Figure 3.3). Setting $Q = 0.9$ as a limit for successful alignment, the alignment time becomes $\tau_0 = t(Q = 0.9) \approx 3\tau$ and Equation (3.12) reads

$$\tau_0 = \frac{\beta}{SB^2}, \ \beta \approx \frac{18\eta\mu_0}{\Delta\chi}. \tag{3.20}$$

Considering the PDLCE's specifications (η, $\Delta\chi$, S), it holds that $\beta/\mathrm{S} \leq 10^3\,\mathrm{sT}^2$. The alignment time to reach $Q = 0.9$ thus varies from $\tau_0 \approx 15\,\mathrm{min}$ for $B = 1\,\mathrm{T}$, to relatively quick $\tau_0 \approx 15\,\mathrm{s}$ at $B = 9\,\mathrm{T}$.

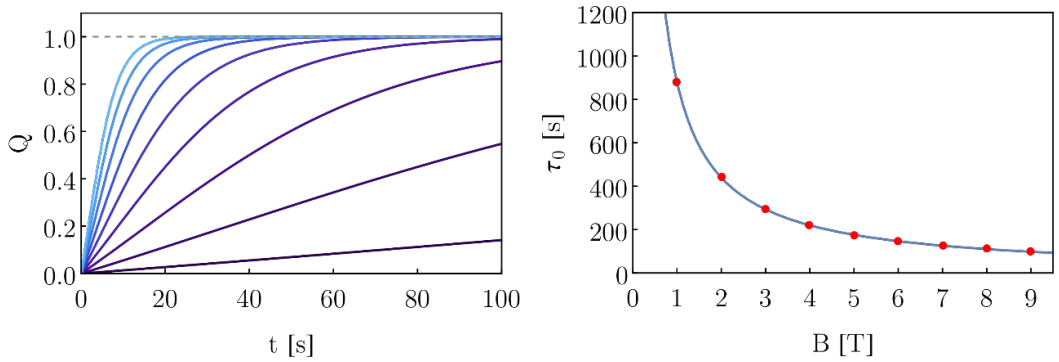


Figure 3.3: Order parameter Q and alignment time τ_0. Estimates of time evolution of order parameter Q for different magnetic fields, i.e. from 9T – bright blue, to 1T – dark blue (Left graph) and alignment timescales in respect to the magnetic field (Right graph). Red dots mark the values at ticked magnetic fields for easier reading.

Chapter 4

Nuclear Magnetic Resonance

4.1 Nuclear Spin Hamiltonian

Nuclear magnetic resonance (NMR) spectroscopy is very useful for investigation of LC systems, since it enables the measurement of molecular dynamical properties through nuclear spin interactions originating from nuclei in LC molecules and their intermolecular interactions. NMR spectroscopy can be performed only on nuclei with a spin different from zero, i.e. when there is an odd number of protons or neutrons in a given nucleus. Nonzero spins give way to discrete energy states when under the influence of an externally applied static magnetic field. NMR spectroscopy is based on this principle, using radiofrequency (RF) pulses to excite the nuclear spin angular momentum between different quantum states and measuring the response of magnetic transitions between energy levels. These are additionally shifted by the interactions of nucleus with its surroundings, from which information of the measured system can be deducted. Quantum description of a system is done by writing a Hamiltonian for each individual process with quantum chemical calculations and adding them together to define the system's total energy. In a LC system, the full Hamiltonian consists of [14]

$$H = H_Z + H_{CS} + H_D + H_Q . \tag{4.1}$$

These are the Hamiltonians for the Zeeman interaction (H_Z), chemical shift (H_{CS}), nuclear dipole-dipole interaction (H_D) and nuclear quadrupole interaction (H_Q). Depending on the LC system, certain interactions prevail and dictate the behavior of energy levels.

Focusing on the first term, the Zeeman interaction describes the influence of a static magnetic field B_0 on the magnetic moment of the nucleus, μ [14], [32], [33]:

$$H_Z = \mu B_0 = -\gamma \hbar m B_0 . \tag{4.2}$$

The gyromagnetic ratio is denoted by γ, describing the ratio between the nucleus' magnetic moment and its angular momentum. $\hbar$ is the reduced Planck constant and m the magnetic quantum number, where values of m run from $-I$ to $+I$ in steps of unity. I denotes the spin of the nucleus. In a static magnetic field, the spin angular momentum vector can exist in different quantum states, separated by energy levels. NMR spectroscopy uses RF waves to induce transitions between the states. A resonance will occur when radiation at Larmor frequency (ω_L) is applied, corresponding to energy levels of

$\Delta H_Z = \hbar\omega_L$ needed to change the magnetic quantum number by $\Delta m = 1$. Considering this, the Larmor frequency is determined by Equation (4.2):

$$\omega_L = \gamma B_0 . \tag{4.3}$$

Other terms (H_{CS}, H_D, H_Q) of the full Hamiltonian arise from the interactions of the nucleus with the surrounding matter. The chemical shift, H_{CS}, originates from orbiting electrons, producing local magnetic fields in the vicinity of the nucleus and causing a small shift of the resonance frequencies. The chemical shift is proportional to the applied magnetic field, so it is more apparent in higher fields, but for LC systems this term is usually overshadowed by other interactions. Nuclei that are closer together exert an influence on each other's effective magnetic field with their nuclear magnetic moments. This interaction is called the dipole-dipole interaction, denoted by the dipolar Hamiltonian, H_D. In liquids this interaction averages out, but for ordered systems, this effect is characterized by the splitting of the observed spectral line or the so-called Pake pattern shape of the spectra. NMR investigations of LCs done on protons (^{1}H), where the dipole-dipole interactions dominate, yield spectra that are a superposition of spectral lines contributed by all of the hydrogen atoms in the molecule. Considering LCEs, this would also mean contributions from H-atoms in the polymer network. It is therefore practical to label mesogen molecules with deuterated sites. Interactions between deuteron sites give rise to the quadrupole interactions (H_Q) from which energy contributions prevail over dipolar, making this technique useful for targeted investigations of orientational and dynamical properties of LCs, since the contributions of the surrounding matter in the measured deuterium NMR spectra are suppressed.

4.2 Quadrupole Interaction

Quadrupole interactions are present only in nuclei with $I > 1/2$. Such spins do not possess spherical symmetry and, due to the distribution of the electronic charge, a non-spherical symmetry electric field gradient is formed at the site of the nucleus. Quadrupole interaction thus arises from interaction of the electric quadrupole moment eQ^* with the formed electric field gradient (EFG). The quadrupolar Hamiltonian H_Q is defined as [14], [32], [33]

$$H_Q = \frac{1}{6}\sum_{\alpha,\beta} V_{\alpha\beta} Q^*_{\alpha\beta} . \tag{4.4}$$

$V_{\alpha\beta}$ denotes the various derivatives of the electric potential, which are the elements of the EFG tensor,

$$V_{\alpha\beta} = \frac{\partial^2 V}{\partial r_\alpha \partial r_\beta}, \tag{4.5}$$

where r_α and r_β are the spatial coordinates and indices $\alpha, \beta = x, y, z$ denote separate components. Notation $Q^*_{\alpha\beta}$ is the quadrupolar coupling tensor which, after applying the Wigner-Eckart theorem [33] to evaluate its matrix elements, takes the operator form of

$$Q^*_{\alpha\beta} = e\sum_k 3r_{\mathrm{k},\alpha}r_{\mathrm{k},\beta} - \delta_{\alpha\beta}r_k^2, \tag{4.6}$$

with k being the number of protons in a given system. Applying the same theorem, eQ^* is defined to be:

$$eQ^* = < I\!I \mid e\sum_k 3r_{k,z}^2 - r_k^2 \mid I\!I >, \tag{4.7}$$

with $m = I$ and Q^* being the quadrupole moment of the nucleus (notation * is added not to be mistaken with order parameter Q).

For an arbitrary orientation of the rectangular coordinates $\alpha = x, y, z$, the Hamiltonian H_Q is written as [33]

$$H_Q = \frac{eQ^*}{6I(I-1)}\sum_{\alpha,\beta}V_{\alpha\beta}\left[\frac{3}{2}(I_\alpha I_\beta + I_\beta I_\alpha) - \delta_{\alpha\beta}I^2\right]. \tag{4.8}$$

The H_Q can be simplified by choice of a set of principal axes for the EFG tensor. Considering also the Laplace's equation $\sum_\alpha V_{\alpha\alpha} = 0$, H_Q can be rewritten into:

$$H_Q = \frac{eQ^*}{4I(2I-1)}\left[V_{zz}(3I_z^2 - I^2) + (V_{xx} - V_{yy})(I_x^2 - I_y^2)\right]. \tag{4.9}$$

H_Q can now be transformed into a laboratory system with a static magnetic field applied in the z'-axis. Taking that in such a system $V_{xx} = V_{yy}$, the Hamiltonian becomes

$$\begin{aligned} H &= H_Z + H_Q = \\ &= -\gamma\hbar B_0 I_{z'} + \frac{e^2qQ^*}{4I(2I-1)}(3I_z^2 - I). \end{aligned} \tag{4.10}$$

q is defined as the field gradient, taken from relation $V_{zz} = eq$.

Perturbation theory is now applied for the quadrupolar coupling, which is here assumed to be weaker in comparison to the magnetic interaction. When the z-axis of the EFG tensor is tilted by angle ϑ against the magnetic field (z'-axis), the perturbed quadrupole Hamiltonian with magnetic number m now reads [33]:

$$H = -\gamma\hbar B_0 m + \frac{e^2qQ^*}{4I(2I-1)}\left[3m^2 - I(I+1)\right]P_2(\cos\vartheta). \tag{4.11}$$

For deuterium, which has spin $I = 1$, the allowed magnetic numbers m are -1, 0 and 1. Therefore, when the deuterium nucleus is under the applied magnetic field, the Zeeman interactions term yields three separate energy levels with the same energy gap in between (Figure 4.1). If there is no quadrupole moment, the resulting spectra is seen as a single line. For a non-zero quadrupole moment, the energy levels are additionally shifted, this time resulting in two different energy gaps. The measured spectrum is now seen as a doublet, with a quadrupole splitting of

$$\Delta\nu = \frac{E_Q}{h} = \frac{3}{2}\nu_Q P_2(\cos\vartheta), \tag{4.12}$$

where the constant $\nu_Q = e^2 qQ^*/h$ is the quadrupolar frequency.

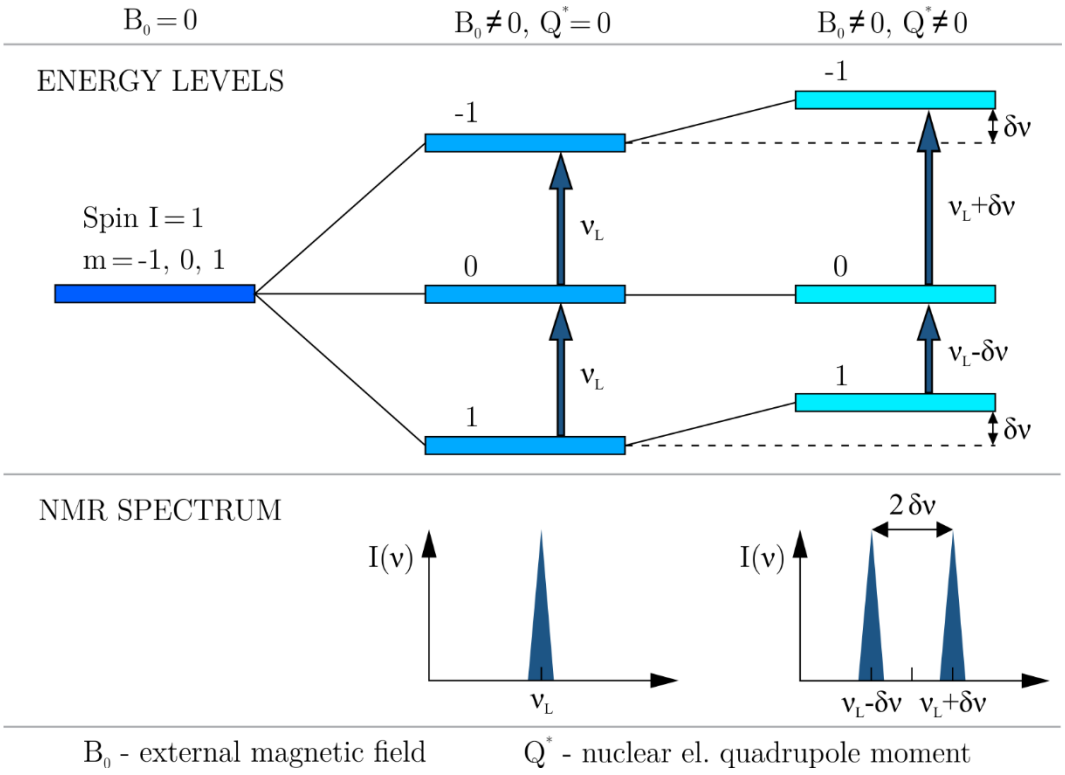


Figure 4.1: Energy levels of a spin 1 nucleus. After the applied magnetic field, the three allowed magnetic numbers ($m = -1, 0, 1$) are split by the same energy gap into three energy levels, yielding a single spectral line. If the quadrupole moment is non-zero, the energy levels are additionally shifted, resulting in different energy gaps between the levels. The spectrum is thus a doublet.

4.3 ^{2}H-NMR of Liquid Crystals

The obtained LC spectra are governed by interactions of the nuclear quadrupole moment with the EFG tensor of the C-^{2}H bond. The interactions are intramolecular in nature and so the ordering of the LC molecules can be extracted from the spectra, i.e. from the quadrupole spectral splitting that can be related to the local order parameter S, as will be described later on.

The EFG tensor points in the direction of the C-^{2}H chemical bond, but due to the molecular rotation around its long molecular axis at rates that are much faster than the quadrupole frequency shifts, it is averaged out on the NMR timescale and the effective EFG tensor takes the direction of the long molecular axis. This process is called motional narrowing. For the deuterated M(D)6 mesogen that was used in the experiments, the deuteration sites are located at the phenyl ring, with the C-^{2}H bond tilted by $\beta = 60°$ against the long molecular axis. The effective EFG tensor is therefore reduced by

$$\mathrm{P}_2(\cos\beta_{C-^2H}) = \mathrm{P}_2(\cos 60°) \approx -\frac{1}{8}, \tag{4.13}$$

so that the average quadrupole frequency for the M(D)6 mesogen deuterated on the phenyl ring now becomes [34]

$$\bar{\nu}_Q = \frac{e^2qQ^*}{h} P_2(\cos\beta_{C-^2H}) = \frac{1}{8}\frac{e^2qQ^*}{h} \approx 22\,\mathrm{kHz}\,. \tag{4.14}$$

The tilting motion or orientation of the long molecular axis can be described by the order tensor $\hat{S}$, in which the off-diagonal terms become zero when the order tensor's eigenframe is chosen to lie in the molecular frame. The relationship of the diagonal terms S_{xx}, S_{yy} and S_{zz} to the quadrupole splitting is given by [14], [35], [36]

$$\Delta\nu = \pm\frac{3}{4}\bar{\nu}_Q S_{zz}\left[\frac{1}{2}(3b_z^2 - 1) + \frac{\eta}{2}(b_x^2 - b_y^2)\right], \tag{4.15}$$

where the unit directional vector $\mathbf{b}$ defining the magnetic field direction is written in the $\hat{S}$ eigensystem and $\eta = S_{xx} - S_{yy}$. The η parameter describes the biaxiality of the molecule and can be omitted for uniaxial mesophases, such as is the case for M(D)6. One can see from this equation that the degree of quadrupolar splitting is directly proportional to the local order parameter at the nucleus site. The term S_{zz} can now be substituted with the local nematic order parameter S_N to yield:

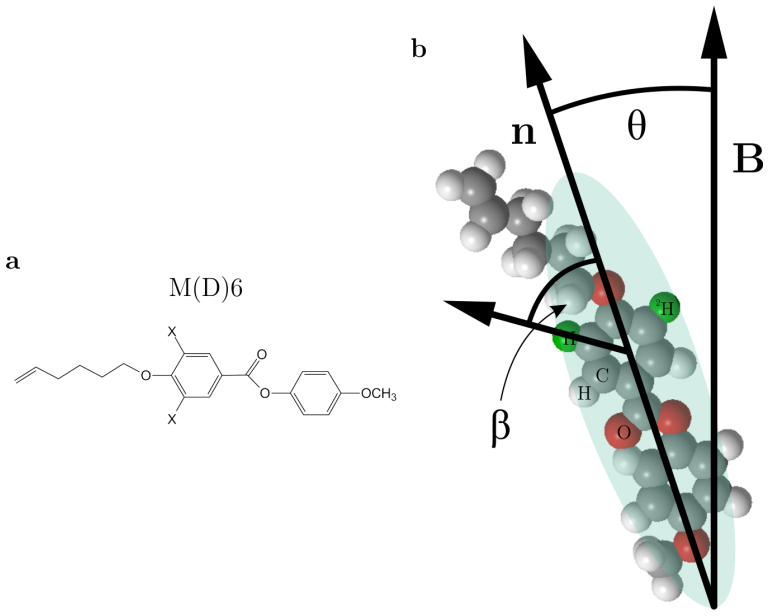


Figure 4.2: Deuterated mesogen M(D)6 and its position against the magnetic field. The M(D)6 mesogenic molecule is additionally labeled with deuterium at the benzene ring, denoted by X in the molecule schematic (a). The order parameter is described by the angle θ between the nematic director $\mathbf{n}$ and the magnetic field $\mathbf{B}$ (b). The nematic director is pointing along the molecular long axis due to motional averaging of the EFG tensor, instead of along the C-^{2}H bonds (tilted by $\beta = 60°$ against the molecular axis).

$$\Delta\nu = \pm\frac{3}{8}\bar{\nu}_Q S_N \left[3\cos^2\theta - 1\right], \tag{4.16}$$

with θ being the tilt of the molecular long axis against the magnetic field. This equation enables the measurement of the orientational order parameter and director alignment of LC systems by means of ^{2}H-NMR spectroscopy.

Chapter 5

Experimental Methods

5.1 LCE Preparation

All the constituents used for the LCE preparation are shown in Figure 5.1. LCEs are composed of a *hydroxymethyl-polysiloxane* polymer chain, to which side-mesogenic units are attached. For nematic LCEs, a nematogen *4-methoxyphenyl 4-(but-3-en-1-yloxy) benzoate* (denoted M4) and in case of smectic LCEs, smectogen *4-methoxyphenyl 4-(undec-10-en-1-yloxy) benzoate* (denoted M11) was used. The polymer chain is interconnected with *1,4-bis (undec-10-en-1-yloxy) benzene* cross-linker molecules (V1) forming a side-chain LCE.

LCE film samples were prepared using the two step Finkelmann procedure [8]. The first step consists of partially crosslinking the LCE material and then using a mechanical field in the form of adding weights, to align the mesogen directors, which is then imprinted in the elastomer by further crosslinking in the second crosslinking step. In this way, the introduced LC anisotropic order is coupled with the polymer network, generating thermomechanical deformations related to phase transition-induced changes in the orientational order.

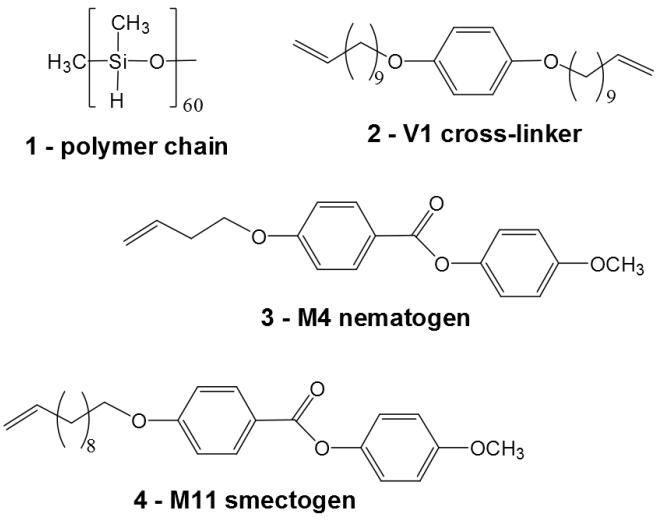


Figure 5.1: Compounds used in the synthesis of LCE systems: (1) Hydroxymethyl-polysiloxane polymeric chain, (2) flexible cross-linker V1, (3) nematogen M4 and (4) smectogen M11.

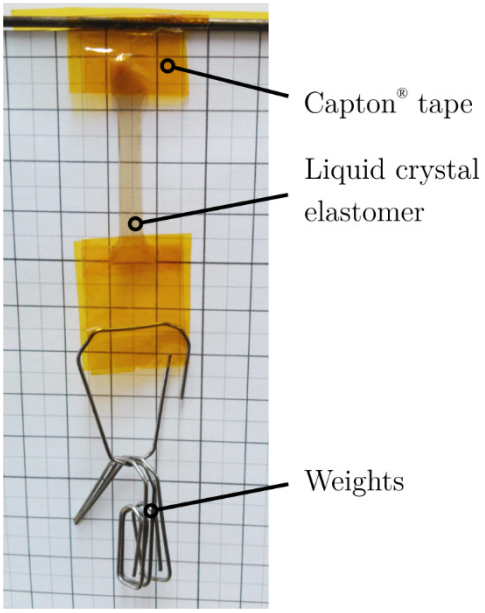


Figure 5.2: Director alignment using a mechanical load. Partially crosslinked LCEs are freely suspended and a hook is taped on the bottom end, onto which weights are added to mechanically align the nematic director. LCEs are then put in an oven to complete the crosslinking process.

A detailed synthetization procedure is now described. LCE film samples were synthesized by adding 1 mmol of Hydroxymethyl-polysiloxane, 15 %mmol of V1 cross-linker and 85 %mmol of mesogen, to 2 ml of anhydrous toluene. 30 μl of saturated Pt-catalyst was added to the mixture and the content was filtered into a home-made cylindrical form for centrifugation. The Pt-catalyst solution was saturated to prevent possible solution concentration changes due to solute evaporation when stored for future synthetizations. The pre-polymerization mixture was centrifuged at 5500 rpm at 70° C for 1h 10min, resulting in a partially cross-linked LCE film. The second reaction step consisted of cutting the LCE film into shorter strips and mechanically loading them at room temperature. Weights of 3 mg were gradually added until the LCE sample became either completely transparent or no further elongation was seen, usually at loads of 15 mg . The samples were left to dry at room temperature for approximately 2 hours and further cross-linked in an oven at 60°C overnight.

A partially ordered bulk LCE material was also synthesized using an applied magnetic field in order to instill mesogen alignment. With this synthetization process, the yielded LCE material is not monodomain, as it is the case with the two-step procedure, but it consists of multiple ordered domains. These are much larger than in a polydomain LCEs, where the aligning process is omitted so that the only ordering that mesogen molecules exhibit is through their intermolecular interactions. It will be demonstrated by experiments that this is indeed the case. The magnetic synthetization amounts of components are completely the same as described in the two-step method. Instead of filtering the prepared LCE pre-polymerization mixture into a cylindrical form, it is here filtered into two 1.2 ml flasks, which are then tightly sealed. They are then mounted on an NMR probe and opened slightly to allow for slow evaporation of toluene. The probe is inserted into the magnet and the two samples are heated to $T = 70°\,\mathrm{C}$ in order to start the polymerization process. The magnet in our case was a superconducting magnet with $B = 11.74\,\mathrm{T}$ magnetic field (Bruker Advance III 500 MHz high-resolution solid-state NMR spectrometer). It is left

overnight to completely polymerize. The flasks are then broken and the LCE material removed, sliced into thin (~ 1 mm) pieces, and put in an oven at 60° C for 24h, for the toluene to completely evaporate.

5.2 PDLCE Preparation

A liquid crystal elastomer is first cut into smaller pieces (approximately 1×1 mm) to prepare for freeze fracturing. The pieces are mixed with PDMS (polydimethylsiloxane – Sylgard® 184 Silicon Elastomer Kit) in a 3:1 weight ratio and put in a mortar. Liquid

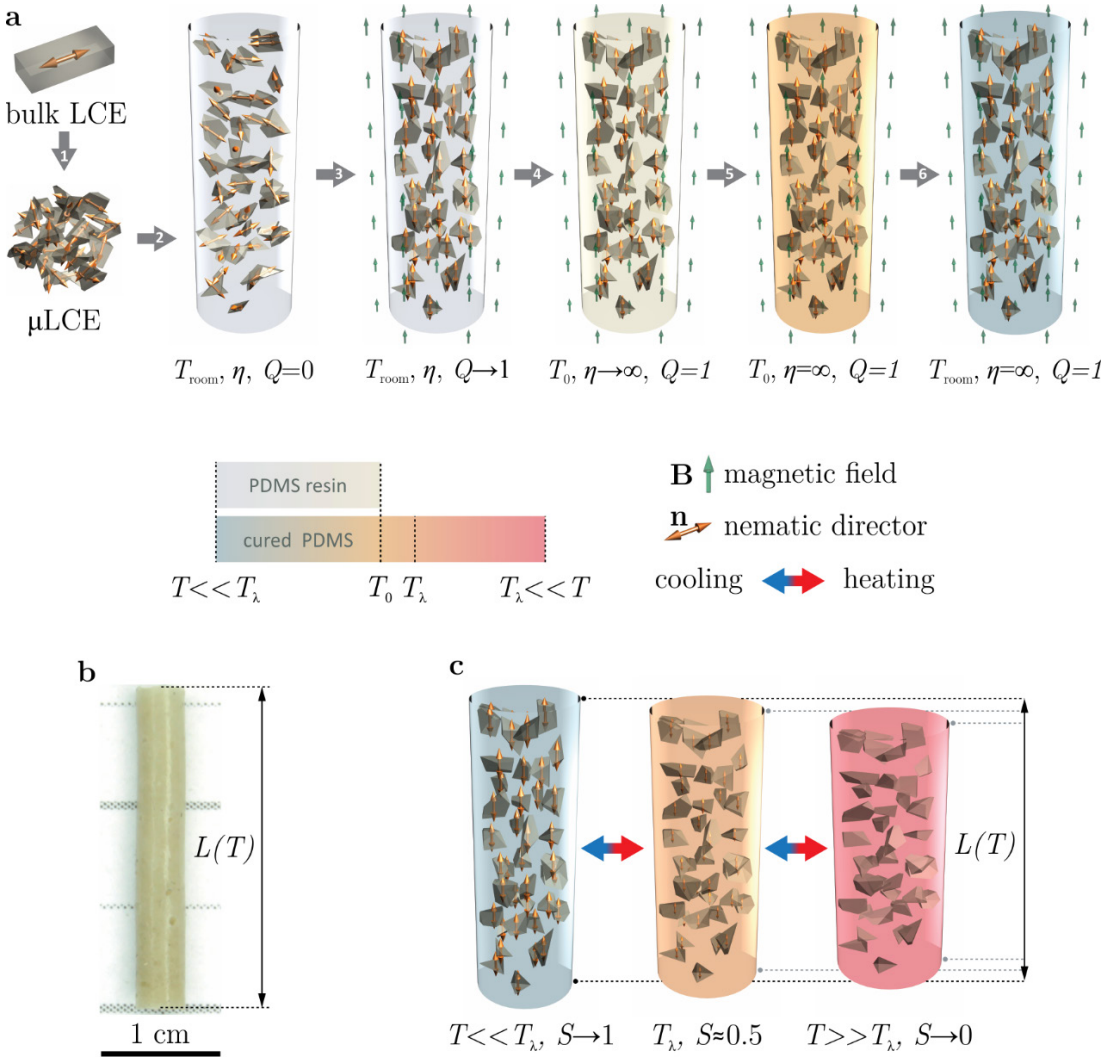


Figure 5.3: PDLCE preparation sequence. (a) Crushed μLCEs are dispersed into a PDMS resin (step 1-2), which is then put into a magnetic field where the particles orient along the field direction (step 3). Upon μLCE alignment, the composite is heated to setting temperature T_0 to polymerize the PDMS matrix (step 4-5). The cured PDLCE is then cooled down and later removed from the magnetic field (step 6). The resulting PDLCE samples were cylindrical in shape and about 1.5 cm long (b). After heating above the activation temperature T_λ, the nematic order parameter of μLCEs is reduced and the resulting TM response is transferred to the surrounding PDMS matrix, forcing the whole composite to deform (c).

nitrogen is repeatedly poured over the melt until visibly frozen and then crushed with a pestle until the mixture thaws. This process is repeated until a homogeneous paste is obtained and is then left at room temperature to dry off water condensation.

The LCE-PDMS mixture is further mixed with PDMS in a required weight ratio, usually $m_{LCE} : m_{PDMS} = 1:1$. The curing agent (Sylgard® 184 Silicon Elastomer Curing Agent) is pipetted into the mixture and mixed. The volume of added curing agent was calculated based on the desired mixing ratio (normally $R_{mix} = m_{CA} : m_{PDMS} = 1:45$ curing agent to base ratio) and the density of the curing agent, $V_{CA} = \mathrm{R}_{mix} m_{PDMS} / \rho_{CA}$, with $\rho_{CA} = 0.893\,\mathrm{mg}/\mu\mathrm{l}$. The prepared mixture is evacuated to get rid of entrapped air. Using a spatula, the mixture is carefully introduced into a glass tube ($4.5\,\mathrm{cm}$ long with $3\,\mathrm{mm}$ inner diameter), minimizing eventual air entrapment. The inside of the tube is covered with a thin Teflon foil to prevent PDMS adhesion to the glass surface. The partially filled tube is then sealed on both sides with a Teflon tape. The sample is put into the bore of $B = 9\,\mathrm{T}$ superconducting magnet with the tube oriented parallel to the magnetic field and left for two hours at room temperature. During this time, the µLCE particles orient themselves so that the µLCE's nematic director is pointing along the direction of the magnetic field. After two hours, the sample is left to cure in the magnet overnight (approximately 12 hours) at $60°\,\mathrm{C}$, well below the N-I transition temperature.

5.3 Thermomechanical and Stress-Strain Measurements

Thermomechanical (TM) and stress-strain measurements were both performed in a home-built setup (Figure 5.4), which consisted of a heating chamber with the investigated sample suspended inside and fixed with Capton® tape on both ends between two metal holders.

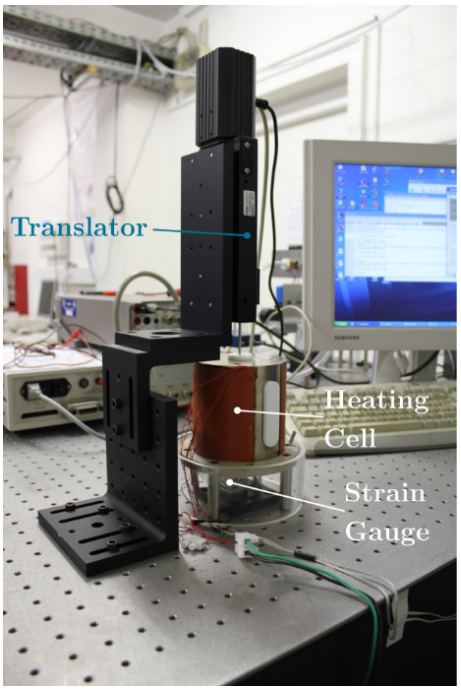


Figure 5.4: Experimental setup for thermomechanical and stress-strain measurements. The sample is located in the middle of the heating cell and attached to the translator at one end and to the strain gauge at the other end. TM and elastic properties are determined by measuring the samples' strain and applied load at a given temperature.

One holder was attached to the translator stage, while the other onto a strain gauge. All LCE samples were ribbon-shaped with typical dimensions $15-20\,\mathrm{mm}\times 3\,\mathrm{mm}\times 0.3\,\mathrm{mm}$. When measuring PDLCE samples, two small square metal plates were glued at each end of the cylindrical PDLCE sample and attached to metal holders with the same Capton® tape. PDLCEs were usually $25\,\mathrm{mm}$ long with $2.8\,\mathrm{mm}$ diameter. Nematic director $\mathbf{n}$ was aligned along the long edge of both LCE and PDLCE samples, with the degree of elongation/contraction measured in the same direction. They were suspended with a constant weight of $100\,\mathrm{mg}$ or equivalent stress of $\sigma_{LCE}=1.1\,\mathrm{kPa}$ for LCEs and $\sigma_{PDLCE}=0.2\,\mathrm{kPa}$ for PDLCEs, respectively, to prevent torsion or bending of the sample. This weight was small enough not to induce any additional elongation.

Thermomechanical response was measured in the constant stress regime ($\sigma_{LCE}=1.1\,\mathrm{kPa}$ and $\sigma_{PDLCE}=0.2\,\mathrm{kPa}$), by heating and subsequent cooling down of the sample in the range $25^\circ\mathrm{C}$ to $105^\circ\mathrm{C}$ ($140^\circ\mathrm{C}$ for smectic samples) at the rate of $0.5^\circ\mathrm{C/min}$. The upper temperature limit was at least $20^\circ\mathrm{C}$ above the N-I transition.

Stress-strain measurements were performed at room temperature ($25^\circ\mathrm{C}$), measuring elongation and relaxation of the specimen over an applied load interval of $100\,\mathrm{mg}$ to $2000\,\mathrm{mg}$ ($1.1\,\mathrm{kPa}$ to $13.1\,\mathrm{kPa}$ for LCEs and $0.2\,\mathrm{kPa}$ to $4\,\mathrm{kPa}$ for PDLCEs) with the load rate slow enough for a linear response to be measured.

5.4 ^{2}H-NMR Measurements

Measurements were performed with a Bruker Advance III 500 MHz high-resolution solid-state NMR spectrometer, equipped with 11.74 T Bruker Ultrashield superconducting magnet at the Larmor frequency of 76.753 MHz for deuterons. Special PDLCE samples were made with µLCEs fabricated from magnetically synthesized LCE material containing phenyl ring-labeled *4-methoxyphenyl 4-(hex-5-en-1-yloxy) benzoate* (denoted M(D)6) deuterated mesogen. The deuterated sites enable one to obtain quadrupole perturbed deuterium NMR spectra, from which the degree of µLCE's orientational distribution and the order parameter can be determined.

Temperature-dependent spectra of the prepared samples were recorded in the temperature range between $360\,\mathrm{K}$ (87 °C) and $300\,\mathrm{K}$ (23 °C), in steps of $5\,\mathrm{K}$ (13 values) for all samples. Temperature was controlled within $0.1\,\mathrm{K}$ accuracy with $5\,\mathrm{min}$ for temperature equilibration between each measurement.

Spectra were recorded by applying a quadrupole echo sequence (90° - τ - 90° - τ_2 - ACQ) with a 90° pulse length of $4.8\,\mu\mathrm{s}$. Echo delay time τ was set from $640\,\mu\mathrm{s}$ to $2.5\,\mu\mathrm{s}$ with decreasing temperature, and delay τ_2 was set to zero. Recycle delay between consecutive acquisitions was set to $25\,\mathrm{ms}$, with 30720 scans performed at each measurement.

5.5 List of LCE Samples

LCE materials used in this study are denoted with LCE-X, where X labels the constituents of LCEs, listed in Table 5-1. The crosslinking procedures are marked with $\star$, $\star$B, $\star\star$ and $\star\star\sigma$. Single star notation $\star$ signifies a one-step crosslinking process performed in an oven, while the additional character B ($\star$B) denotes the same one-step process performed under the influence of an external magnetic field of $B=12\,\mathrm{T}$. Double star notation $\star\star$ is used for the Finkelmann two-step synthesis procedure [9], where the elastomer is partially crosslinked in a temperature-controlled centrifuge and then further crosslinked in an oven

while being freely suspended. If the sample is aligned by an applied mechanical load in the second crosslinking step, it is additionally denoted by index σ (⋆⋆σ). Maximum deformation responses ($\lambda(\mathrm{T})_{\max}$) of synthesized LCE samples were determined by TM measurements, except for ⋆ and ⋆B, which produced deformed bulk LCE material, unsuited for measurements. Also listed in Table 5-1 are the µLCE's domain types. Both procedures, ⋆B and ⋆⋆σ, yield partially oriented or oriented LCEs which, when freeze-fractured, result in monodomain µLCEs. LCE material synthesized without any applied field to orient the LCE material, ⋆ and ⋆⋆, consists of many randomly oriented domains. When crushed, these can yield either polydomain or monodomain particles, depending on the µLCE's nematic (or smectic) domain sizes. If both are in the range of microns to tens of microns, µLCEs consist of multiple domains and exhibit only a small effective nematic order S_N. Particles of nanometer sizes, on the other hand, consist of a single domain and the order parameter of the µLCE is well defined. This implies that an efficient fracturing process can always yield monodomain µLCEs, regardless of the LCE material synthetization process.

Table 5-1: List of LCE material used for PDLCE preparation.

LCE label	*%wt M4*	*%wt M11*	*%wt M(D)6*	*Average* $\lambda(\mathrm{T})_{\max}$	*Crosslinking*	*µLCE label*	*µLCE domains*
LCE-A	100	-	-	1.45	⋆⋆σ	µLCE-A	mono
LCE-Ap	100	-	-	1.00	⋆⋆	µLCE-Ap	poly/mono
LCE-B1	50	35	-	1.38	⋆⋆σ	µLCE-B1	mono
LCE-B2	17	68	-	1.32	⋆⋆σ	µLCE-B2	mono
LCE-C	100	-	-	-	⋆B	µLCE-C	mono
LCE-Cp	100	-	-	-	⋆	µLCE-Cp	poly/mono
LCE-D	25	-	60	1.40	⋆B	µLCE-D	mono

Chapter 6

PDLCE Characterization and Optimization

6.1 Thermomechanical Response of PDLCE Species

The type of μLCE inclusions used in PDLCE preparation has a significant role in determining the degree of composite's TM response. Since the transfer of mechanical fields, arising from μLCE's deformations, onto the composite is partially suppressed by the TM inactive polymer matrix, it is important that the μLCE material exhibits high TM deformation. This is achieved by using a combination of starting LCE materials that yields a high enough TM response. Additionally, the LCE material and, more importantly, corresponding μLCEs must consist of well-defined domains for the orientational process to be successful and for the particles to experience unidirectional deformation. TM response of PLDCEs based on different types of μLCEs inclusions and synthetization processes (listed in Table 6-1) was therefore measured to determine what LCE material is best suitable for composite preparation in order to provide for adequate response.

Table 6-1: List of all PDLCE samples.

PDLCE label	*μLCE composition*	*B during setting*	*μLCE order parameter*	$\lambda(\mathrm{T}_{room})$
PDLCE-A	μLCE-A	9T	$Q \to 1$	1.12
PDLCE-Ap	μLCE-Ap	9T	$0 < Q < 1$	1.045
PDLCE-A-iso	μLCE-A	-	$Q = 0$	0.975
PDLCE-Ap-iso	μLCE-Ap	-	$Q = 0$	0.975
PDLCE-B	μLCE-B1, μLCE-B2 (1:1)	9T	$Q \to 1$	1.09
PDLCE-C	μLCE-C	9T	$0 < Q < 1$	1.065
PDLCE-Cp	μLCE-Cp	9T	$0 < Q < 1$	1.02
PDLCE-D*	μLCE-D	Variable	$Q \to 1$	n.a.

* were only used for ^{2}H-NMR experiments

TM strain responses for all investigated PDLCE species are plotted in Figure 6.1. PDLCEs that have been aligned using $9\,\mathrm{T}$ magnetic field are denoted with full lines, whereas the non-oriented ones are denoted with dashed lines. Samples with $Q > 0$ show a decrease in $\lambda(\mathrm{T})$ at around $T = 80\,^{\circ}\mathrm{C}$, in a similar manner as in regular LCEs. Non-functionalized PDMS sample was also measured for comparison, which exhibits

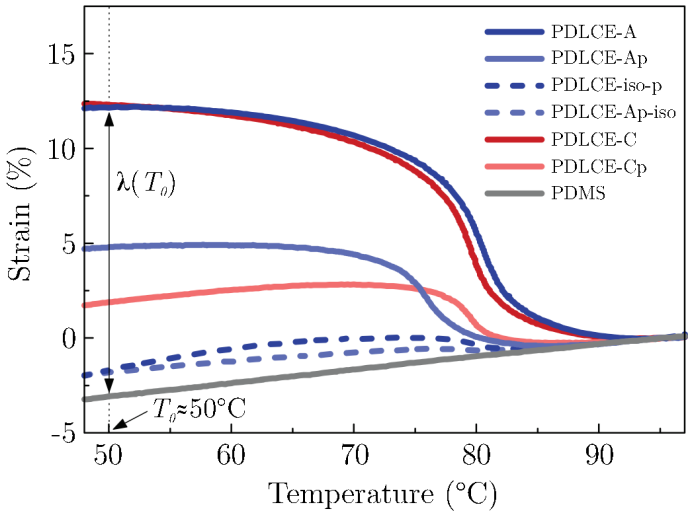


Figure 6.1: Thermomechanical responses, $\lambda(\mathrm{T}) = \mathrm{L}(\mathrm{T})/\mathrm{L}(\mathrm{T}_{ref})$ with $T_{ref} = 95\,^{\circ}\mathrm{C}$, of various PDLCE species, shown as strain percentage $100(\lambda - 1)$. Maximum strain is exhibited by oriented (full lines) composites with μLCEs made of mechanically and magnetically aligned material (PDLCE-A and PDLCE C), while the PDLCE-Ap and PDLCE-Cp exhibit weaker response, suggesting that their μLCE inclusions consist of multiple domains. Non-oriented (dashed lines) PDLCE-A-iso and PDLCE-Ap-iso both have an anticipated negative TM response. All strain outputs are compared at $T_0 = 50\,^{\circ}\mathrm{C}$.

conventional linear thermal expansion of $\lambda_{PDMS}(\mathrm{T}_0) \approx 0.965$. Isotropic samples ($Q = 0$), i.e. PDLCE-A-iso and PDLCE-Ap-iso, display only a small residual deformation of $\lambda(\mathrm{T}_0) \approx 0.975$, originating from randomly oriented μLCEs. Considerably larger response is observed in oriented samples PDLCE-Cp and PDLCE-Ap, $\lambda(\mathrm{T}_0) \approx 1.019$ and $\lambda(\mathrm{T}_0) \approx 1.048$, respectively. Compared to their oriented analogues, PDLCE-A ($\star\star\sigma$ μLCEs) and PDLCE-C ($\star$B μLCEs), they exhibit smaller TM deformation, suggesting that the μLCEs are polydomain. Such μLCEs are oriented in the direction of the particle's mean nematic director and since individual domains are randomly oriented, there is loss in the particle's unidirectional deformation. Maximum strain of the PDLCE is reduced accordingly, but is still higher than for the non-aligned PDLCEs (see PDLCE-A-iso and PDLCE-Ap-iso), since the μLCEs are oriented at least to some extent.

The highest strains can thus be observed for PDLCE-A and PDLCE-C with $\lambda(\mathrm{T}_0) \approx 1.122$ and $\lambda(\mathrm{T}_0) \approx 1.123$, respectively. A high degree of deformation for PDLCE-A is not surprising, since they include μLCEs made of monodomain LCEs ($\star\star\sigma$). It is therefore expected that the μLCEs themselves are of monodomain nature and the highest strain output should be possible only for such particles. But it is surprising that PDLCE-C delivers almost the same TM profile, suggesting that the introduced magnetic field during LCE synthetization process ($\star$B) produces considerately larger domains, such that the LCE material can be grinded down to single domain μLCEs. This realization has a rather big implication on the production of PDLCEs, meaning that the Finkelmann procedure ($\star\star\sigma$) can be altogether bypassed, or most importantly, the tedious second step where one must align the partially crosslinked LCEs by adding weights. Although the $\star\star\sigma$ process produces nicely shaped rectangular LCE films, which are very useful for research, it cannot yield a large enough amount for any other purposes, like industrial scale

production. By employing ⋆B synthetization, one can produce practically any desirable amount of LCE material. And even though the resulting LCE has no particular shape, it is later milled into μLCEs and remolded into custom shapes in the form of a PDLCE. This synthetization process requires no special handling or skill and therefore grants PDLCEs a large potential for industrial implementation by its practicality and production yield. It also confirms that with an efficient milling process one can produce monodomain μLCEs from partially aligned LCEs. A further particle size reduction down to sub-micron levels would result in single-domain particles obtained from polydomain LCE material (with domain sizes of $\sim 10^{-7}$ m [6]), thus even abandoning the need for an alignment field during the LCE material synthesis.

By using different fillers one can custom tailor PDLCE's TM and elastic properties or even add additional functionality to the composite. To demonstrate this, two different LCE materials were used, each with its own transition temperature, to produce a PDLCE with bimodal TM behavior (Figure 6.2). Elastomers used for this purpose were LCE-B1 and LCE-B2 with transition temperatures at $T_{\lambda,1} = 87\,°\mathrm{C}$ and $T_{\lambda,2} = 114\,°\mathrm{C}$, respectively. Both LCEs were crushed into microparticles and made into a PDLCE-B sample with 50 %wt μLCE concentration, consisting of 25 %wt μLCE-B1 and 25 %wt μLCE-B2. The resulting PDLCE-B composite exhibits two successive TM deformations, something that cannot be achieved with LCEs by simply using different types of constituents – the resulting LCE still exhibits only a single TM response with the transition temperature determined by a combination of mesogenic molecular properties and their concentrations. This can be clearly seen in both LCE-B1 and LCE-B2 (Figure 6.2-a) consisting of two, M4 and M11 mesogens, but at different ratios. PDLCE-B's effective response, on the other hand, is a superposition of both μLCE responses, which amounts to $\lambda(\mathrm{T}) = k_1\lambda_1(\mathrm{T}) + k_2\lambda_2(\mathrm{T})$, with

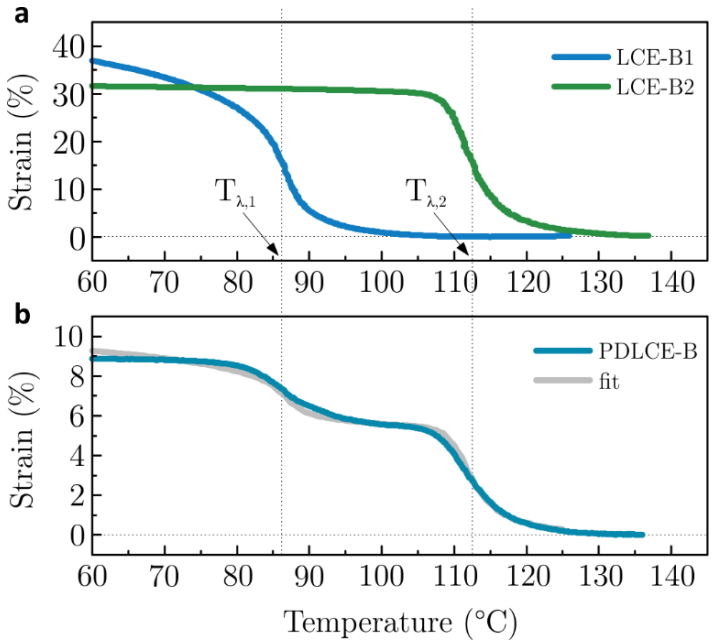


Figure 6.2: Two-step PDLCE composite. Plotted are the two TM profiles of LCE-B1 and LCE-B2 elastomers, each exhibiting a different transition temperature (a), and the strain output of PDLCE-B composite (b) made from corresponding μLCE-B1 and μLCE-B2. The composite shows a bimodal response, which is a superposition of both LCE responses. The gray line denotes the optimal fit given by linear superposition. model.

k_1 and k_2 being the weights of respective individual μLCE types. When fitted to PDLCE-B's TM profile (Figure 6.2-b, grey line), the optimal fit yields $k_1 = 0.1$ and $k_2 = 0.18$. Since strain output differs only about ~5% in the two LCEs, the fact that $k_2 > k_1$ can be attributed to much higher Young's modulus of LCE-B2 ($E_2 = 3.2\,\text{MPa} \gg E_1 = 230\,\text{kPa}$) on behalf of a higher smectogen component concentration.

6.2 Investigation of PDLCE's Structure

Investigations of PDLCE structural characteristics were carried out under a polarizing optical microscope. PDLCE-A sample with 5 %wt concentration of μLCE-A was made and cut into 0.1 mm thin slices along the alignment director. The slices were first imaged with optical microscope without polarizers to see the structural composition and to obtain an estimation of the particle size distribution (Figure 6.3). Dark spots in Figure 6.3-a are μLCE particles imbedded into the polymer matrix, which is transparent, with the faint abrasion marks resulting from slicing the specimen. When the sample is imaged using

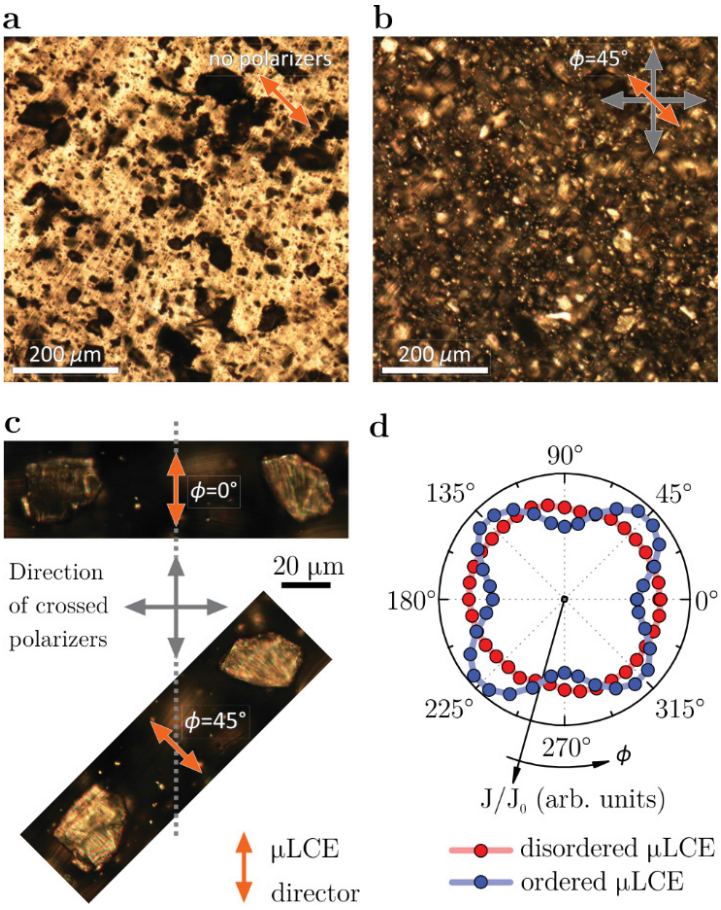


Figure 6.3: PDLCE structure under a polarizing optical microscope. LCE particles are blackened without polarizers (a) and appear bright between two crossed polarizers (b). The orientation of LCEs can be determined from the brightness of polarized image - intensity is maximal when the director of the particle is at 45° angles with respect to both polarizers. This can be seen when observing individual particles (c) or measuring the integral intensity modulation of the image at different angles (d).

crossed polarizers (Figure 6.3-b) the μLCE appears bright due to additional polarization of light by birefringent mesogenic molecules in μLCE. Particle sizes can be estimated from both images, ranging from sub-micron sizes to a few ten microns. Despite the relatively wide particle size distribution, their dispersion appears homogenous without any significant aggregations.

Since the nematic director $\mathbf{n}$ is well defined for monodomain μLCE-A, their orientation can be determined from the brightness of polarizing light transmitted through the particles. When the sample is rotated against the crossed polarizers, the brightness changes and is maximal when the particle's director is at 45° angle with respect to polarizers, as demonstrated for the pair of micro-particles in Figure 6.3-c. With this approach, one can determine whether μLCE particles exhibit any orientational ordering, by rotating the sample and measuring the integral intensity of transmitted light. Regarding the PDLCE-Ap sample with 5 %wt μLCE concentration, it is clearly seen in Figure 6.3-d that the intensity is more or less constant, i.e., independent of rotation angle, whereas, on the other hand, it is modulated for the case of ordered PDLCE-A sample. This is a clear proof that particles indeed exhibit some orientational ordering. Quantitatively, the degree of ordering cannot be reliably determined using the above procedure.

6.3 Modeling of PDLCE's Elastic and Thermomechanical Properties

Prediction on the PDLCE's TM response can be made by describing a bilayer composite in terms of alternating layers of thermomechanically active LCE and inert PDMS matrix materials. These layers can be stacked in series (denoted s) or in parallel (denoted p) in respect to the orientation of LCE's nematic director $\mathbf{n}$. When considering the series scenario, the stress on both materials is the same, whereas for the parallel scenario, the overall strain in the composite is distributed between the two materials. By writing the μLCE volume fraction as $\nu = V_{LCE}/(V_{LCE} + V_{PDMS})$, the relations for the series case read,

$$\sigma = \nu\sigma_{LCE} + (1-\nu)\sigma_{PDMS} \tag{5.1}$$

and

$$\varepsilon = \nu\varepsilon_{LCE} + (1-\nu)\varepsilon_{PDMS} \tag{5.2}$$

for the parallel case. Abiding by the Hooke's law, respective elastic moduli along director $\mathbf{n}$ can now be expressed [37]:

$$E_s = E_{LCE}/(\nu + (1-\nu)\,\mathrm{y}) \tag{5.3}$$

and

$$E_p = E_{LCE}(\nu + (1-\nu)\,\mathrm{y})\,, \tag{5.4}$$

with $y = E_{LCE}/E_{PDMS}$ being the relative elastic modulus. One can now proceed with the calculation of the corresponding TM responses, $\lambda_s(T)$ and $\lambda_p(T)$, using Figure 6.4 as reference. It depicts the geometry of the LCE and PDMS layers and their deformation for both the series (Figure 6.4 a) and parallel (Figure 6.4 b) scenarios.

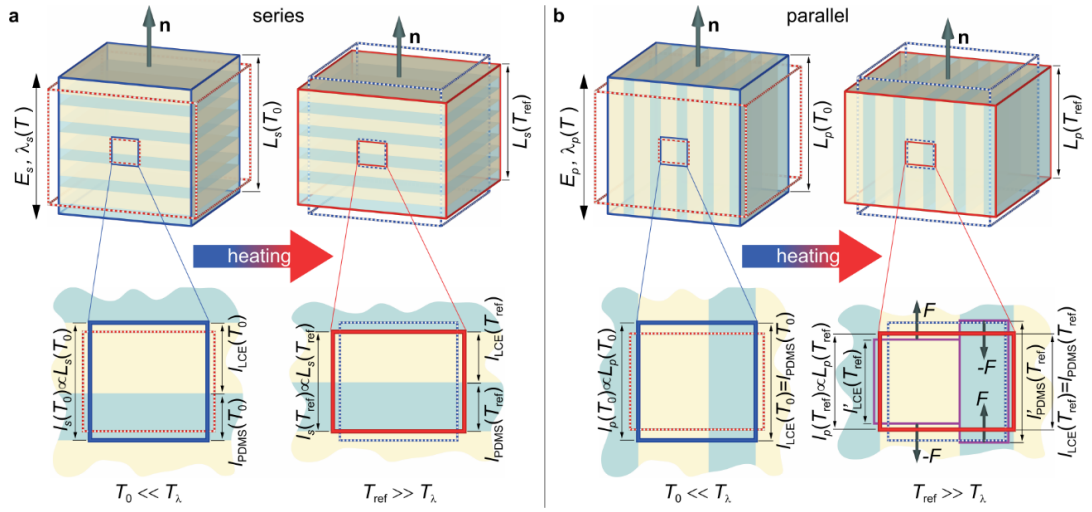


Figure 6.4: Layer geometry for the series and parallel model. LCE and PDMS layers are stacked in series (a) and parallel (b) against the nematic director $\mathbf{n}$. A square containig one layer of each material is chosen at T_0 to calculate the composite's TM deformation response. In both cases, the layers contract in the $\mathbf{n}$ direction and expand perpendicularly with the rising temperature.

A PDLCE exhibits no internal stresses at the setting temperature T_0. The sample length is denoted by $L_{s,p}(T)$ for each case, with each layer being of length $l_{LCE}(T)$ and $l_{PDMS}(T)$. At T_{ref}, the LCE layers contract in the $\mathbf{n}$ direction and exert stress upon the PDMS layers, thus deforming the whole PDLCE sample, which also expands along the direction perpendicular to $\mathbf{n}$. A square region containing a single LCE and PDMS layer (Figure 6.4, solid line frames) is selected at T_0 for calculation purposes. Geometry changes in the direction perpendicular to $\mathbf{n}$ are disregarded since the cross-section areas of the selected region (A_{LCE} and A_{PDMS}) are independent of T. Deformation of each unconstrained layer in the $\mathbf{n}$ direction is described by $L_{LCE}(T)$ and $L_{PDMS}(T)$, and the effective length of the composite layer can be described by

$$L_s(T) = \mathrm{L}_{LCE}(T) + \mathrm{L}_{PDMS}(T) \tag{5.5}$$

and

$$L_p(T) = \mathrm{L}_{LCE}(T) = \mathrm{L}_{PDMS}(T) \tag{5.6}$$

for the series and parallel models, respectively. Here, the thermally induced force $F(T)$ is acting on both layers and results in internal stresses of $\sigma_{LCE} = F(T)/\mathrm{A}_{LCE}$ and $\sigma_{PDMS} = F(T)/\mathrm{A}_{PDMS}$. The length of each layer is thus changed by $L(T) = l'(T) + \Delta l'$. At T_0, the $l'(T_0)$ is the same for LCE and PDMS layers, $l'_{LCE}(T_0) = l'_{PDMS}(T_0)$, but at a higher temperature each material deforms differently. The lengths are therefore compensated by $\Delta l'$, resulting from internal stresses σ_{LCE} and σ_{PDMS} with forces acting in opposite direction for each material (see Figure 6.4 b), thus yielding

$$L_{LCE}(T) = l'_{LCE}(T)\left[1 + \frac{\sigma_{LCE}}{E_{LCE}}\right] \tag{5.7}$$

and

$$L_{PDMS}(T) = l'_{PDMS}(T)\left[1 - \frac{\sigma_{PDMS}}{E_{PDMS}}\right]. \tag{5.8}$$

The TM response is now defined at the reference temperature T_{ref}, chosen high above the T_{NI} transition temperature in order to take into account the large TM deformation of μLCE particles. The effective response of the composite is written as

$$\lambda(T) = \frac{L(T)}{L(T_{ref})}, \tag{5.9}$$

which comprises of individual material responses given by

$$\lambda_{LCE}(T) = \frac{L_{LCE}(T)}{L_{LCE}(T_{ref})} \tag{5.10}$$

and

$$\lambda_{PDMS}(T) = \frac{L_{PDMS}(T)}{L_{PDMS}(T_{ref})}. \tag{5.11}$$

The μLCE volume fraction,

$$\nu = \frac{V_{LCE}}{V_{LCE} + V_{PDMS}} = \frac{A_{LCE}L_{LCE}(T_0)}{A_{LCE}L_{LCE}(T_0) + A_{PDMS}L_{PDMS}(T_0)} \tag{5.12}$$

can be written for the series scenario,

$$\nu_s = \frac{L_{LCE}(T_0)}{L_{LCE}(T_0) + L_{PDMS}(T_0)} \tag{5.13}$$

and, by assuming T-independency, $A_{LCE} = A_{PDMS}$, the parallel scenario volume fraction is given by

$$\nu_p = \frac{A_{LCE}(T_0)}{A_{LCE}(T_0) + A_{PDMS}(T_0)}. \tag{5.14}$$

With all equations set, the TM responses for both scenarios can now be calculated. By substituting $L(T)$ in relation (5.9) with the effective length L_s (5.5) and also taking into account the individual LCE and PDMS responses, (5.10) and (5.11), with $L_{LCE}(T_0)/L_{PDMS}(T_0) = \nu/(1-\nu)$ calculated from (5.13), the TM response for the series model $\lambda_s(T)$ can be obtained. The calculation of $\lambda_p(T)$ for the parallel model is performed

in a similar way, by using L_p (5.6) instead of $L(T)$ and deriving $A_{LCE}/A_{PDMS} = \nu/(1-\nu)$ from (5.14). The results for both cases are:

$$\lambda_s(T) = \frac{\nu\lambda_{LCE}(T)\lambda_{PDMS}(T_0) + (1-\nu)\lambda_{LCE}(T_0)\lambda_{PDMS}(T)}{\nu\lambda_{PDMS}(T_0) + (1-\nu)\lambda_{LCE}(T_0)} \tag{5.15}$$

and

$$\lambda_p(T) = \frac{(1-\nu)\lambda_{PDMS}(T_0) + y\nu\lambda_{LCE}(T_0)}{(1-\nu)\lambda_{PDMS}(T_0)/\lambda_{PDMS}(T) + y\nu\lambda_{LCE}(T_0)/\lambda_{LCE}(T)}. \tag{5.16}$$

These two results can be applied to any binary composite comprising of elastic compounds and not only to PDLCEs. The requisites for calculating TM responses for both cases are the knowledge about the PDLCE composition ν, the relative modulus y and the setting temperature T_0. These calculations have been used to generate theoretical curves to compare against measurements presented in the next chapter.

6.4 Optimization of PDLCE Properties

A simple quantitative analysis was made to optimize TM and elastic properties of PDLCE composites, to see how to maximize PDLCE's degree of deformation, while also obtaining the highest Young's modulus possible. For most applicative purposes it is important that the composites possess high elastic constant to match those of the passive rubber elements used in most practical cases, which are at least in the ~MPa range and above. Since our LCEs are rather soft ($E \approx 60\,\text{kPa}$), their effective deformation can be quite suppressed by using a stiffer PDMS matrix. To get the most response from PDLCEs, besides achieving the highest Q possible, the matrix should either possess Young's modulus lower or equal to that of the LCE's or the LCE material should exhibit a high initial TM response.

In order to optimize PDLCE properties, several PDLCE-A samples with varying µLCE concentrations were prepared to test the amount of µLCEs needed to achieve the highest strain output possible. The initial LCE material used in PDLCE-A exhibited $\lambda_{LCE}(T_0) = 1.4 \pm 0,05$ strain and Young's modulus of $E_{LCE} = 60 \pm 6\,\text{kPa}$. PDMS matrix material was held constant at $E_{PDMS} = 180 \pm 15\,\text{kPa}$ for the purpose of concentration dependency measurements. Samples with constant µLCE concentration, but with different PDMS matrix stiffness, were also fabricated to measure the interplay between E_{PDMS} and composite's TM deformation. The results are given in Figure 6.5.

They demonstrate how PDLCE material can be custom-tailored to exhibit different TM deformations and different Young's moduli by varying the LCE fraction ν (Figure 6.5 a and c) or the relative elastic modulus $y = E_{LCE}/E_{PDMS}$ (Figure 6.5 c and d). With increasing ν the effective modulus is linearly reduced from initial $E \approx 180\,\text{kPa}$ of the PDMS matrix to values of $E \approx 60\,\text{kPa}$ of the LCE material. PDLCEs at higher LCE fractions ($\nu > 0.60$) also become less stable due to µLCEs concentration exceeding the percolation level. Variations in the effective modulus are attributed to experimental error of E_{PDMS}. It is evident that the modulus will be reduced by doping a harder PDMS matrix with much softer LCE material, with the effective values reaching individual component modulus at the opposite concentration limits. By reducing the relative modulus at constant ν, the modulus decreases exponentially, reaching the E_{LCE} value for $y \to 1$. It is seen

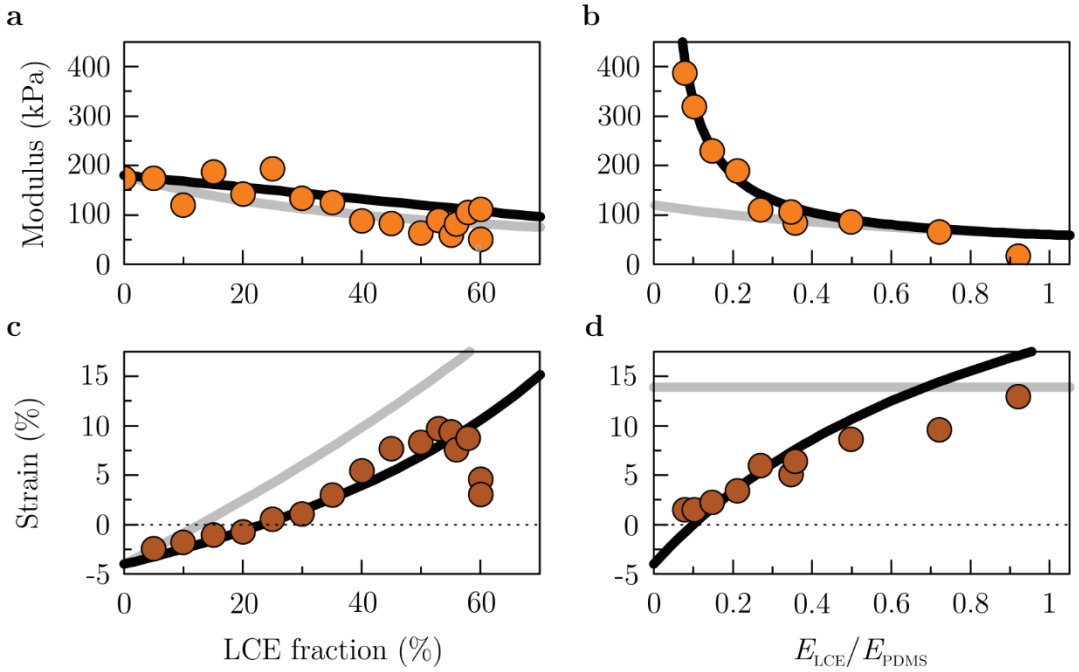


Figure 6.5: Optimization of PDLCE properties. PDLCE's modulus (a and b) and strain (c and d) have been measured with respect to the LCE fraction ν and relative elastic modulus, $y = E_{LCE}/E_{PDMS}$. Modulus is reduced with higher LCE concentration, while the maximum response is increased. Strain decreases abruptly at $\nu > 0.50$ due to the percolation of µLCEs. PDLCE's modulus is governed by E_{PDMS} and is decreasing on $y \to 1$. The maximum TM response is achieved at $\sim 50\,\%$wt LCE fraction and when $E_{PDMS} \leq E_{LCE}$. Gray and black lines are predictions from the series and parallel models, described in Section 6.3.

that the overall modulus is dictated by the much stiffer PDMS matrix. For $y \approx 1$ ($y > 0.94$ in our case), the PDMS matrix is too soft to produce a stable PDLCE so that experimental values could not be determined.

Focusing on the strain outputs for different ν (Figure 6.5 d), one can see that the strain increases on raising LCE fraction until it reaches the maximum of $12\,\%$ at $\nu = 0.50$. The steep sudden drop in strain at $\nu > 0.60$ can be again attributed to the percolation of µLCEs, which prevents alignment of the particles when oriented in the magnetic field. At low LCE fraction, the strain is even negative and becomes positive only at $\nu \approx 0.30$, demonstrating the predominant role of PDMS stiffness in the effective PDLCE properties when the LCE modulus is low. This is also visible in Figure 6.5 d, where the strain increases to a maximum value of $14\,\%$ when the PDMS modulus is close to that of the µLCEs ($y \to 1$). At $y \to 0.05$ only a slight anomaly in the TM curve is seen, amounting to about $\sim 1\,\%$ strain. At even lower values, PDMS matrix is too stiff to result in a detectable positive effective strain.

In section 6.3, two models to describe the overall elastic modulus of PDLCE composites and their associated TM deformations as a function of relative modulus y and LCE fraction ν were developed. When comparing theoretical predictions against measurements, one can see that the parallel model results are in particularly good agreement with experiments. There are some discrepancies, especially considering the TM deformation

responses (Figure 6.5 c and d), which are due to the percolation of the filler particles and sample stability degradation at low PDMS concentration, these having been disregarded in the model. The series model fails to describe the measurements. Real life scenario is a combination of serial and parallel configuration, but for practical predictions of PDLCE's properties, the parallel model seems to be adequate.

Experimental points of Figure 6.5c suggest that the highest strain is achieved in the range of $40-60\,\%\text{wt}$ LCE fraction with PDMS modulus close to LCE's at $60-100\,\text{kPa}$. For PDLCE-A, the optimum values would be $50\,\%\text{wt}$ LCE fraction at $E \approx 100\,\text{kPa}$ overall Young's modulus, yielding $\lambda(T_0) = 1{,}12$ maximum strain. This is a rather modest output, considering that the initial LCE-A material exhibits $\lambda_{LCE-A} \approx 1{,}4$. But since PDLCEs impose almost no restriction on the choice of matrix or filler materials, one can find many substitute materials to achieve higher effective TM response of $\lambda \approx 1.15$ and modulus values of $E \approx 1\,\text{MPa}$. A straightforward choice would be main-chain μLCEs as fillers, which have a high strain output of $\lambda(T_0) \approx 2$ and $E \approx 1\,\text{MPa}$ [38]. Such PDLCE would result in an excellent thermomechanical and elastic performance ($\lambda(T_0) > 1.5$ and $E > 1\,\text{MPa}$), making the composite appealing for many applicative purposes.

6.5 Effect of Setting Temperature on the PDLCE Response

It was shown that the PDLCE's TM responses are strongly dependent on the LCE filler fractions and material properties of both the filler and the surrounding matrix. But the degree of TM output is also clearly affected by the amount of μLCE's orientational order. Unsuccessful alignment leads to degradation of TM responses, be it due to multi-domain nature of the LCE particles or due to insufficient strength of the magnetic field in which they are aligned. Another factor affecting the response is also the nematic order parameter S_N of μLCEs, which is governed by temperature. While thermally setting (polymerizing) the uncured PDLCE, it is advisable that the setting temperature is kept below the N-I transition of the particles, so that the μLCE's nematic director, required to be nonzero for successful orientation, is well defined. If this is not the case, then the alignment time diverges ($\tau_0(S \to 0) \to \infty$), e.g. in the isotropic phase, as was shown in section 3.4, and the alignment process is ineffective. Materials at hand, used for the PDLCE production, enabled the polymerization of the composite's matrix well below the N-I transition temperature, but for materials with high setting temperature, this may not be possible. Therefore, the role of setting temperature T_0 must be assessed.

For this purpose, only the parallel model (Section 6.3) will be considered, which was shown to be superior to the series scenario in reproducing our experimental data. The temperature dependence of $\lambda_{LCE}(T)$ and $\lambda_{PDMS}(T)$ can be written for the combined length changes originating from mesogen ordering $\Delta L^{(S)}(T)$ and material's thermal expansion $\Delta L^{(\alpha)}(T)$. The responses are:

$$\lambda_{LCE}(T) = \frac{L_{LCE}(T_{ref}) + \Delta L^{(S)}_{LCE}(T) + \Delta L^{(\alpha)}_{LCE}(T)}{L_{LCE}(T_{ref})} = \\ = 1 + \gamma Q S_N(T) + \alpha_{LCE}(T - T_{ref}) \tag{5.17}$$

and

$$\lambda_{PDMS}(T) = \frac{L_{PDMS}(T_{ref}) + \Delta L^{(\alpha)}_{PDMS}(T)}{L_{PDMS}(T_{ref})} = \\ = 1 + \alpha_{PDMS}(T - T_{ref}), \tag{5.18}$$

where α is the thermal expansion constant and the term $\gamma S_N(T)$ describes the coupling between the orientational order of the nematogen molecules $S_N(T)$ and the polymer backbone [13]. γ can be determined experimentally from the relation $\gamma = \lambda_{LCE}(T(S \to 1)) - 1 - \alpha_{LCE}(T(S \to 1) - T_{ref})$. Since PDMS does not exhibit nematic ordering, the term $\gamma S_N(T)$ is omitted. Equation (5.17) also contains the order parameter Q, which describes the collective orientation of µLCE particles inside the PDLCE (Section 3.3). This order parameter is used to describe the cases when µLCEs are not perfectly aligned. Even though Q is a property of the PDLCE, not the µLCEs themselves for which Equation (5.17) applies, it properly reproduces the PDLCE's behavior, since the term Q renormalizes the µLCE's nematic order parameter S_N for randomly oriented µLCEs. As anticipated and demonstrated experimentally, PDLCE's response is insensitive to S_N when $Q = 0$.

Both $\lambda_{LCE}(T)$ (5.17) and $\lambda_{PDMS}(T)$ (5.18) can now be inserted in the parallel model (Section 6.3 - (5.16)) to determine the PDLCE's response. The thermal expansion constant for both materials can be calculated from Figure 6.1 (Section 6.1), providing values of $\alpha_{PDMS} \approx \alpha_{LCE} \approx 7 \times 10^{-4}\ \mathrm{K}^{-1}$. TM properties of µLCE-A yield that $T(S_N \to 1) \approx \mathrm{T}_{room}$ and $\lambda_{LCE}(T_{room}) \approx 1{,}4$, from which one estimates $\gamma = 0.45$. Since $\alpha(T - T_0) \ll \gamma Q S_N$, the linear thermal expansion can be disregarded ($\alpha_{LCE} = \alpha_{PDMS} = 0$) without much influence on the λ_p(T) prediction, allowing for simplifications $\lambda_{PDMS}(T_0) \approx \lambda_{PDMS}(T) \approx 1$ and $\lambda_{LCE}(T) = 1 + \gamma Q S_N(T)$. One can now calculate the PDLCE's response:

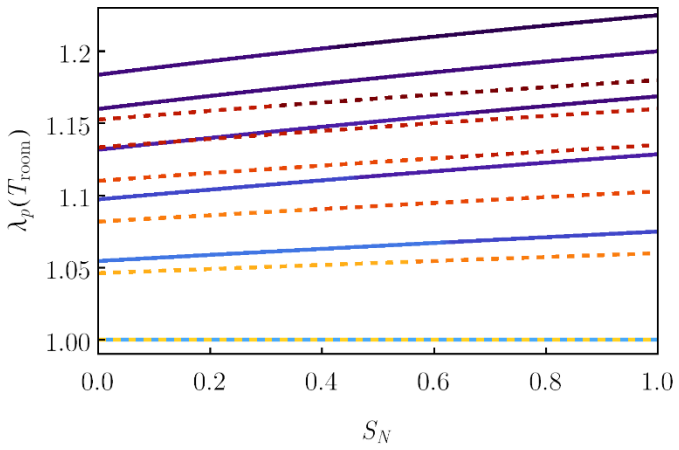


Figure 6.6: PDLCE performance. Graph shows the maximum PDLCE's strain output at T_{room} for different nematic order parameters S_N of µLCEs at the setting temperature T_0. From top to bottom, the lines represent different relative elasticities $y = E_{LCE}/E_{PDMS}$ going from $y =$ 1, 0.8, 0.6, 0.4, 0.2 and 0. Blue lines denote strain performances for a perfectly aligned PDLCE at $Q = 1$ and red dashed lines for partially aligned at $Q = 0.8$.

$$\lambda_p(T) = \frac{(1-\nu) + y\nu\lambda_{LCE}(T_0)}{(1-\nu) + y\nu\lambda_{LCE}(T_0)/\lambda_{LCE}(T)} = \\ = \frac{(1-\nu) + y\nu(1+\gamma QS_N(T_0))}{(1-\nu) + y\nu(1+\gamma QS_N(T_0))/(1+\gamma QS_N(T))}. \tag{5.19}$$

With increasing nematic order $S_N(T)$, i.e. lowering the temperature, the PDLCE's response increases and exhibits a maximum at $S_N = 1$. One can now approximate the maximum $\lambda_0(S_N = 1)$ (found at room temperature T_{room}) for different nematic order parameters S_N at the resin setting temperature T_0. From Figure 6.6 it is seen that $S(T_0)$ only slightly influences the final PDLCE's response, which is mostly governed by the orientation order parameter Q. This means that the PDMS matrix can be cured at any given temperature without significant loss in the final response. It is only important that the alignment process is performed at temperatures below T_{N-I} and that enough time is given for the μLCEs to successfully align. After the alignment, the setting temperature can be chosen in accordance with material specifications.

Chapter 7

^{2}H-NMR Spectroscopy of PDLCE Composites

7.1 Modeling the ^{2}H-NMR Spectra

PDLCE's order parameter Q can be determined by recording and analyzing the quadrupole perturbed NMR spectra of deuterated μLCE mesogen constituents. Since Q describes how well μLCEs are aligned with respect to the external magnetic field, the recorded spectra of PDLCEs mimic the same behavior of quadrupole splitting as for deuterated liquid crystals. Therefore, PDLCE's spectral lines can be treated with the same model as used to describe molecular order of LCE domains, whereas in PDLCEs case, the domain director is analogous to the individual monodomain μLCE's director.

In order to model the NMR spectra, it is presumed that the orientational distribution of an aligned LCE domain's nematic director is a spherical Gaussian and is written as [17], [34], [39]:

$$w(u,\sigma_u) = \frac{e^{-\frac{1-u^2}{2\sigma_u^2}}}{e^{-\frac{1}{2\sigma_u^2}}\sqrt{2\pi}\sigma_u \operatorname{erfi}\left(\frac{1}{\sqrt{2}\sigma_u}\right)}. \tag{6.1}$$

Variable u denotes the orientation angle of a given domain with respect to the magnetic field direction, $u = \cos\theta \in [-1,1]$, and $\sigma_u \in [0,\infty]$ is the degree of dispersion of domain orientation distribution, which can be modelled by $\tan\sigma_\theta = \sigma_u$, where the new dispersion term is expressed in degrees of angle θ inside the interval of $\sigma_\theta \in [0,90°]$. Erfi is the imaginary error function. The global order parameter Q is best determined at lower temperatures where the nematic order parameter S_N is the largest. In this low temperature regime, the transversal relaxation contribution $(-M/T_2)$ and the diffusion term contribution $(D\nabla^2 M)$ to the time-dependence of nuclear magnetization M, given by the solutions of Bloch equations of the magnetization precession ([14], [32], [33]), approaches zero and can be disregarded. The ^{2}H-NMR spectra is thus described only by the resonant frequencies of deuterated mesogens related to the electric quadrupole coupling. The Bloch equations for the magnetization precession in the plane perpendicular to the magnetic field are given by

$$\frac{\partial M}{\partial t} = i2\pi\nu^{\pm} M\,, \tag{6.2}$$

where $\nu^{\pm}$ is the magnetization precession frequency given by Equation (4.16) (Section 4.3) and M is the magnetization. It is convenient to first assume a completely isotropic distribution of domain alignment directions, such as in a polydomain LCE. These are described by a spherical distribution, the surface of which is divided, for the purpose of efficient numerical calculation, by a grid of parallels, $l\,d(\cos\theta) = l\,du$, and meridians, $l\,d\phi$, where l is the sphere radius and θ and ϕ are the azimuthal and polar angles. The problem is discretized by partitioning the spherical coordinate space into N equally spaced coordinates [17], [34]:

$$\begin{aligned} &\phi_k = i\Delta\phi,\ \ \Delta\phi = 2\pi/N \\ &u_j = 1-(j-1/2)\Delta\mathrm{u},\ \ \Delta u = 2/N \\ &M(\phi,u) \to M_{ij} = M(\phi_i, u_j) \\ &\nu^{\pm}(u) \to \nu_j^{\pm} = \nu^{\pm}(u_j) \end{aligned} \tag{6.3}$$

By introducing $M_k = \sum_{i,j=k} M_{ij}$ and performing a summation over index i, one obtains

$$\frac{d\mathbf{M}(t)}{dt} = (i2\pi\underline{\nu}^{\pm})\mathbf{M}(t) = i\underline{\Omega}^{\pm}\mathbf{M}(t), \tag{6.4}$$

where $\mathbf{M}$ is the N-component magnetization vector comprising of magnetization components M_k and $\underline{\Omega}^{\pm} = 2\pi\underline{\nu}^{\pm}$ is the $N\times N$ diagonal matrix of resonant frequencies where $\underline{\nu}^{\pm} = \nu_k^{\pm}\cdot\underline{\mathbf{1}}$. Fourier transformation is applied to relation (6.4) to obtain the intensity vector

$$I^{\pm}(\nu) \propto \int_0^{\infty} e^{-t2\pi\nu\underline{\mathbf{1}}t} M(t) = (\underline{K}^{\pm}(\nu))^{-1}\underline{\mathbf{1}}\,, \tag{6.5}$$

which is the inverse of the matrix $\underline{K}^{\pm}(\nu) = i2\pi(\underline{\nu}^{\pm} - \nu\underline{\mathbf{1}})$. Components of the intensity vectors contain the signal from the interval $u\in[u_k^-, u_k^+]$ where $u_k^- = u_k - \Delta u/2$ and $u_k^+ = u_k + \Delta u/2$. The overall intensity is then calculated as the sum over matrix components,

$$I(\nu) \propto \underline{\mathbf{1}}^{\mathrm{T}}(K^{\pm}(\nu))^{-1}\underline{\mathbf{1}}\,. \tag{6.6}$$

To implement the above model to monodomain LCEs, with high degree of orientational order, the spherical distribution for the isotropic case must be transformed into the spherical Gaussian. This is done by introducing a new variable $v(u,\sigma_u)$ for which the spherical Gaussian distribution is constant. In this way the grid, which was defined on the spherical distribution surface, is remapped on the new surface of the spherical Gaussian. To address the distribution uniformity condition, the new 'isoprobability' variable is calculated to be of the form [17], [34]:

$$v(u,\sigma_u)=\int_{-1}^{u} w(u',\sigma_u)du'=\frac{1}{2}\left[1+\frac{\operatorname{erfi}\left(\frac{u}{\sqrt{2}\,\sigma_u}\right)}{\operatorname{erfi}\left(\frac{1}{\sqrt{2}\,\sigma_u}\right)}\right]. \tag{6.7}$$

The procedure to obtain the frequency spectra is now repeated as for the spherical distribution. The problem is discretized between the $v(u,\sigma_u)\in[0,1]$ range, to obtain N equidistant intervals of $[(k-1)\Delta v,\ k\Delta v]$ as was done for the variable $u\in[-1,1]$ with intervals between $[u_k^-,\ u_k^+]$ and lengths of $\Delta u_k=u_k^+ + u_k^-$. The matrix of the effective magnetization frequencies $\underline{\nu}^{\pm}$ now contains

$$\langle\nu\rangle_k^{\pm}=N\int_{u_k^-}^{u_k^+}\nu^{\pm}(u)w(u,\sigma_u)du\,, \tag{6.8}$$

which are averaged with respective intervals Δu_k with integral limits of $u_k^-=u(v=(k-1)\Delta v)$ and $u_k^+=u(v=k\Delta v)$, with $u(v)$ being the inverse of the function $v(u)$. Fourier transformation is applied to the equation of motion for the magnetization vector (Equation (6.4)), considering also the rewritten $\underline{\nu}^{\pm}$ matrix, in order to calculate the intensity vector required in the calculation of the frequency spectra (Equations (6.5) and (6.6)).

The calculated spectra can be directly used to model the experimental spectral patterns of a sample that is oriented in parallel with the magnetic field so that $u=\cos\theta=1$. This way, the shape of the evaluated spectra is governed only by the value of the dispersion of orientational distribution σ_θ. Once obtained, the σ_θ values can be used to assess the order parameter of domain orientation, which is calculated to be [34]:

$$\begin{aligned}Q(\sigma_\theta)&=\int_{-1}^{1} w(u,\sigma_u)\frac{(3u^2-1)}{2}du\\&=-\frac{1}{2}-\frac{3\sigma_u^2}{2}+\frac{3e^{\frac{1}{2\sigma_u^2}}\sigma_u}{\sqrt{2\pi}\operatorname{erfi}\left(\frac{1}{\sqrt{2}\,\sigma_u}\right)}\\&=-\frac{1}{2}-\tan(\sigma_\theta)\left(\frac{3\tan(\sigma_\theta)}{2}-\frac{3e^{\frac{\operatorname{ctg}^2(\sigma_\theta)}{2}}}{\sqrt{2\pi}\operatorname{erfi}\left(\frac{\operatorname{ctg}(\sigma_\theta)}{\sqrt{2}}\right)}\right).\end{aligned} \tag{6.9}$$

Regarding PDLCEs, the parameter σ_θ describes the dispersion of μLCE's orientations, and since the domain order parameter $Q(\sigma_\theta)$ is related to σ_θ, its evaluation can be used to determine the μLCE's orientational order.

7.2 Sample Preparation

Additional LCEs have been magnetically synthesized (⋆B – see Table 5-1) for the purpose of recording the ^{2}H-NMR spectra, which contained a portion of benzene-ring deuterated M6 mesogens, termed LCE-D (see Table 5-1). Corresponding PDLCE-D composites were prepared from the obtained LCE-D material, which were polymerized under various magnetic fields in the range $B = 1.5 - 9\,\mathrm{T}$. Different magnetic fields were accessed by repositioning the NMR probe away from the $B = 9\,\mathrm{T}$ NMR magnet bore's center using plastic tubular-shaped spacers of various lengths. Composite samples were prepared the same way as described in Section 5.2, with the probe chamber heated beforehand to the setting temperature of $T_0 = 330\,\mathrm{K}$ to immediately initiate the setting process of the uncured sample. This way the µLCE's orientation could be quenched in a semi-oriented state, before their complete alignment, depending on the strength of the magnetic field.

After curing, the PDLCE-D samples were cut in half along the specimen's length, with one part wrapped in a single sheet of Teflon® and inserted into the flat cylindrical coil used for measuring the NMR spectra. The sample was positioned in the center of the coil, perpendicular to the coil axis, so that the nematic director $\mathbf{n}$ was pointing along the magnetic field (see Figure 7.1). Two rolls of Teflon® tape, approximately the same size as the PDLCE sample, were also packed inside the coil at both sides of the sample to prevent the sample from displacing upon deformation and to completely fill the coil.

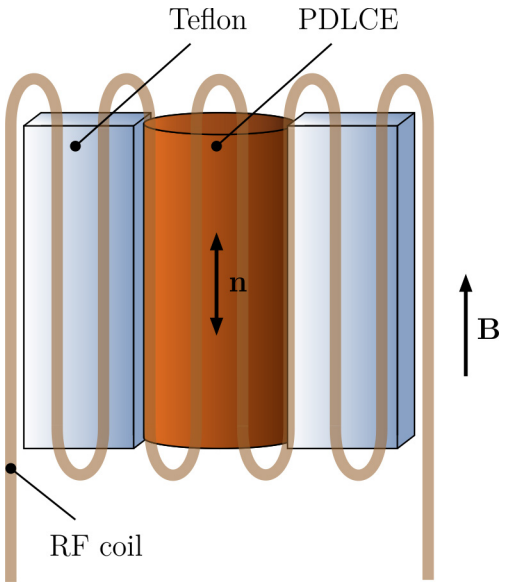


Figure 7.1: PDLCE sample position inside the RF coil. Measured PDLCEs were positioned at the center of a flattened coil with its nematic director pointing along the magnetic field and were tightly fixed in place by two pieces of rolled Teflon sheet at both sides.

7.3 Impact of Viscosity on µLCE Alignment

In Section 3.4, a derivation is made of the time evolution of µLCEs alignment and the associated order parameter Q that is achieved by orienting the µLCE particles in an applied magnetic field. It has been estimated that the time needed to reach a desirable

alignment is around 18 min at $B = 1\,\mathrm{T}$, so the alignment time of 2 h, used in the PDLCE preparation process, was surely long enough to orient all the μLCEs, especially for PDLCEs prepared in $B = 9\,\mathrm{T}$. The alignment process was performed at room temperature where the viscosity of the prepolymer melt is assumed to be time-independent and the μLCE's alignment time τ (Section 3.4, Equation (3.12)) is affected only by the strength of the applied magnetic field. In order to determine the degree of μLCE orientational order in the PDLCE system, the μLCE orientation was quenched in the semi-aligned state. Specifically, this is done by immediately heating the PDLCE sample to the setting temperature ($T_0 = 330\,\mathrm{K}$) to immediately initiate the curing process. During this phase, the viscosity of PDMS melt is increasing until it forms a gel with diverging viscosity, $\eta \to \infty$, resulting in orientational locking of μLCEs. The model derived in Section 3.4 must therefore be rewritten to successfully reproduce the quenched order parameter Q, by taking into account time-dependent viscosity of the matrix.

I have used a two-component Sylgard 184 Silicone rubber as the PLDCE matrix which was mixed in a 1:45 curing agent to base weight ratio. The polymer melt starts to crosslink upon heating and the viscosity increases with time in an exponential manner (see Figure 7.2) [40]:

$$\eta(t) = \eta_0 e^{kt}\,, \tag{6.10}$$

where η_0 is the zero-time, resin viscosity and k the kinetic factor associated with the rate of crosslinking. The kinetic factor was calculated from data taken from reference [41], where the same silicone rubber was investigated at the setting temperature of $T_0 = 330\,\mathrm{K}$, resulting in $k = 0.253\,\mathrm{min}^{-1}$. Although data in [41] refers to a melt with a 1:10 curing agent to base ratio, meaning that the rate of polymerization in our case must be a bit slower, the estimation for k should still hold pretty well.

To evaluate Q, one must again solve the equation of motion (Section 3.4, Equation (3.17)), this time also taking into account time-evolved viscosity $\eta(t)$. The equation of motion is now written as

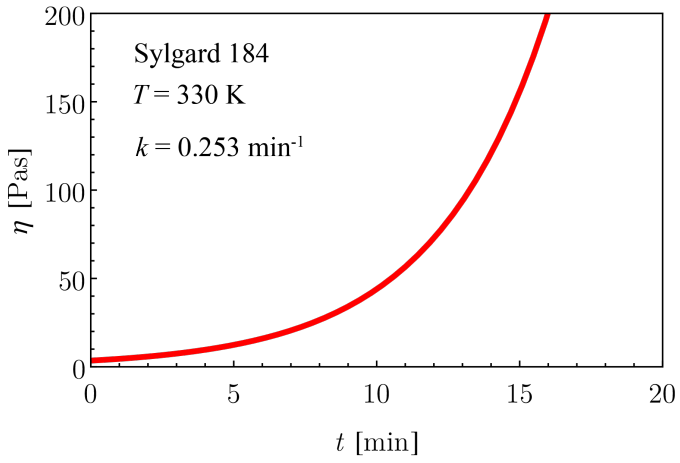


Figure 7.2: Calculated time-dependent viscosity of PDLCE polymer matrix. Upon heating to the setting temperature, the polymer melt starts to crosslink and the viscosity increases exponentially over time until the matrix forms a gel and further polymerizes into an elastomer network.

$$\frac{d\vartheta}{dt} = -\tau_\eta(t)\sin\vartheta\cos\vartheta\,. \tag{6.11}$$

Here, the alignment time $\tau_\eta(t)$ now depends on the time via time-evolved viscosity η(t):

$$\tau_\eta(t) = \frac{6\mu_0\eta(t)}{S\Delta\chi B^2} = \frac{6\mu_0\eta_0}{S\Delta\chi B^2}e^{kt}\,. \tag{6.12}$$

Similar as before, a new characteristic time $\tau_k = 1/k$ is defined, which depends on the kinetic factor of the curing matrix. Taking into account the already defined alignment time τ (see Equation (3.12) in Section 3.4), the equation of motion now rewrites as

$$\frac{d\vartheta}{dt}\tau e^{\frac{t}{\tau_k}} = -\sin\vartheta\cos\vartheta\,, \tag{6.13}$$

and by implementing back the dimensionless time $\tilde{t}$, it takes a simpler form of

$$\frac{d\vartheta}{d\tilde{t}}e^{\tilde{k}\tilde{t}} = -\sin\vartheta\cos\vartheta\,. \tag{6.14}$$

I have defined a new dimensionless factor $\tilde{k} = \tau/\tau_k$, which describes the interplay between the magnetically driven alignment and viscous dampening on the overall particle's alignment time. With the same initial conditions as before, $d\vartheta/d\tilde{t}(\tilde{t}=0) = 0$ and $\vartheta(\tilde{t}=0) = \vartheta_0$, the equation of motion has an analytical solution:

$$\cos\vartheta(\tilde{t},\cos\vartheta_0) = \frac{1}{\sqrt{1+\frac{1-\cos^2\vartheta_0}{\cos^2\vartheta_0}e^{-\frac{2}{\tilde{k}}\left(1-e^{-\tilde{k}\tilde{t}}\right)}}}\,, \tag{6.15}$$

from which the new order parameter $Q(\tilde{t},\tilde{k})$ is derived to be,

$$Q(\tilde{t},\tilde{k}) = -\frac{1}{2\left(e^{2/\tilde{k}\left(e^{-\tilde{k}\tilde{t}}\right)}-1\right)}\left(2+e^{2/\tilde{k}\left(e^{-\tilde{k}\tilde{t}}\right)}-\frac{3\arctan\sqrt{e^{2/\tilde{k}\left(e^{-\tilde{k}\tilde{t}}\right)}-1}}{\sqrt{e^{2/\tilde{k}\left(e^{-\tilde{k}\tilde{t}}\right)}-1}}\right). \tag{6.16}$$

Estimations for the order parameter achieved during the aligning process can now be made and are depicted in Figure 7.3 top graph. The curves were calculated for different magnetic fields running from $1\,\mathrm{T}$ to $9\,\mathrm{T}$ (Figure 7.3 top - blue to orange, respectively). Parameters used in the calculations are the same as the ones used in Section 3.4, except for $\eta_0 = 3.5\,\mathrm{Pas}$ and $S = 0.44$ (taken from experimental analysis in the next chapter), and for including the kinetic factor $k = 0.253\,\mathrm{min}^{-1}$. At the start of the alignment process, the order parameter rises quickly and after some time it saturates when the matrix' viscosity rises enough to completely suppress particle reorientation. For strong fields, i.e. $B > 4\,\mathrm{T}$, a complete alignment can be achieved, meaning that the µLCE's alignment time τ is much shorter than the rate of polymerization. But at smaller fields ($B < 4\,\mathrm{T}$) the alignment time is longer and the particles are only partially aligned before their orientation

is quenched by the high viscosity. The maximum order parameter for our choice of materials is always reached at around $\tilde{t} \approx 9$, independent of the magnetic field.

The interplay between the magnetically driven alignment time τ and the polymerization rate τ_k, as well as their impact on the order parameter, can be resolved from Figure 7.3 - bottom graph, depicting the order parameter $Q(\tilde{k})$ at different dimensionless times $\tilde{t}$ (with values of $\tilde{t} = 0.1, 0.5, 1, 2$ and continuing to 10 in steps of 2 – blue to green, respectively). At the start of polymerization ($\tilde{t} < 1 \Rightarrow t < \tau$), the viscosity is low enough so that the particle alignment is mostly affected by the magnetic torque. The order parameter values are low since the particles have not aligned yet. At longer times, $\tilde{t} > 1$, the order parameter is affected by the rising factor $\tilde{k}$, reducing the maximum order parameter that can be achieved in the system. When the factor $\tilde{k}$ value is low, the particle reorientation is not restricted by the viscosity. At faster polymerization rates

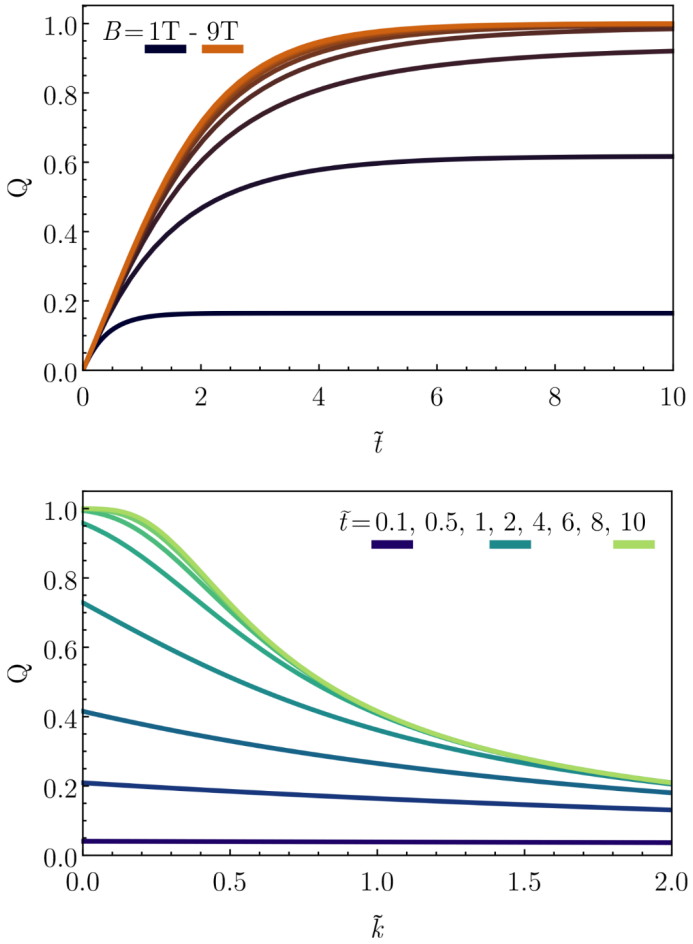


Figure 7.3: Evolution of order parameter Q during the alignment process. μLCEs get completely aligned at higher magnetic fields (top graph – orange), since the alignment time τ is faster than the polymerization rate τ_k. At lower fields ($B < 4\,\mathrm{T}$, dark blue curves), the viscosity locks the particles in place in the semi-aligned state, resulting in a lower saturated value of the order parameter. How well the particles can be aligned is governed by factor $\tilde{k} = \tau / \tau_k$ (bottom graph), which at short times, $\tilde{t} < 1$ (blue curves), only weakly affects the final Q, while at longer $\tilde{t} > 1$, the saturated order parameter drops considerately with $\tilde{k}$, where the μLCEs alignment is again inhibited by the large viscosity of the surrounding matrix.

($\tau_k << \tau$), the viscosity severely hinders particle's reorientation, making complete alignment impossible even at high magnetic fields.

Considering the above facts, the alignment process is best performed when $\tilde{k}$ is sufficiently low, i.e. when the polymerization timescale is much longer than the alignment timescale, $\tau_k >> \tau$. This can be achieved by aligning μLCEs with high magnetic fields at low setting temperatures (where $S \to 1$) or by using a polymer matrix with low viscosity and low kinetic factor so that successful μLCE alignment is possible even at low magnetic fields. Another possibility is to use UV-curable polymer, which can be polymerized by irradiating the material with UV-light. The polymerization process could therefore be triggered when needed so that the problems associated with heat-curable polymers, like the variable viscosity, slow rate of polymerization, and low nematic order parameter at higher temperatures, could all be averted. Unfortunately, the currently available UV-curable PDMS-based polymers are not suitable for our particular case of PDLCE materials because of their high viscosity and inability to control the elastic constant of the cured matrix needed for PDLCE characterization and optimization.

As already stated, the degree of orientational order of cured μLCEs is associated with the maximum value of the order parameter Q attained in the setting process. With this information, one can now predict the resulting PDLCE's order parameter from plotting $Q(B)$ (Figure 7.4) for curing time larger than $\tilde{t} > 9$, when the maximum Q is surely reached. The results show that the maximum order is established at $B > 4\,\mathrm{T}$, where the magnetic field is strong enough to completely align μLCEs before their reorientation is blocked by the matrix's high viscosity. The order parameter is gradually reduced for fields below $5\,\mathrm{T}$, with the μLCE's orientation being completely isotropic if the PDLCE is cured without an applied magnetic field ($B = 0\,\mathrm{T}$). A similar trend is thus expected for the experimentally obtained order parameter $Q(\sigma_\theta)$.

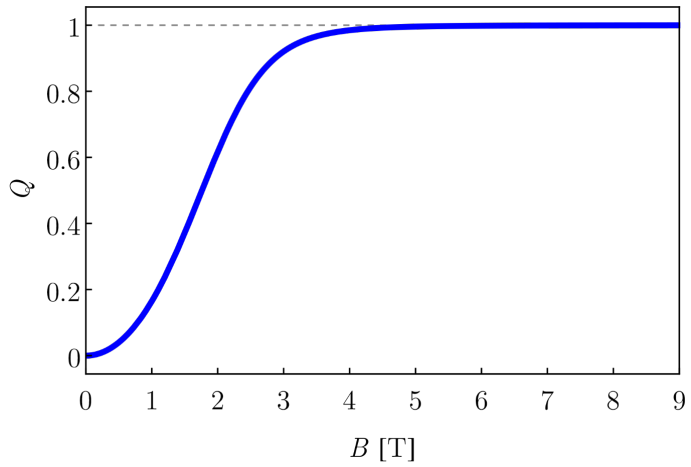


Figure 7.4: Estimated order parameter at different magnetic fields. The calculated PDLCE's order parameter is rising with increasing magnetic field and becomes saturated when the magnetic field is sufficiently large, i.e. at $B > 4\,\mathrm{T}$. The parameters used for the calculation are the same as in Figure 7.3 top graph and with the dimensionless time set to $\tilde{t} = 10$.

7.4 Determining the Orientational Order Parameter Q

Spectra of PDLCEs, prepared under different magnetic fields, were all recorded at the composite's setting temperature ($T_0 = 330\,\mathrm{K}$) to eliminate all internal stresses between the polymer matrix and μLCE particles arising from non-matching strains of both materials when subjected to temperatures different from T_0. These stresses can skew the μLCEs alignment, leading to a false determination of the imprinted order parameter Q. The recorded spectra are given in Figure 7.5 (blue), along with their simulated counterparts (red) computed using the model described in Section 7.1. Measurements show the splitting of the recorded spectra that is characteristic of LC systems. At lower fields, the splitting is minimum with peaks positioned at $\nu = \pm 3\,\mathrm{kHz}$, signifying a random distribution of μLCE's nematic director orientation. Outer peaks positioned at $\nu = \pm 6\,\mathrm{kHz}$ are already formed, indicating that part of the particles are already somewhat aligned in the field direction. The particles' orientational order increases with rising magnetic field, making the outer peaks more pronounced. One can see that the particles become well aligned at $B \geq 5\,\mathrm{T}$, where the outer and inner peaks are of the same general height. Note that the

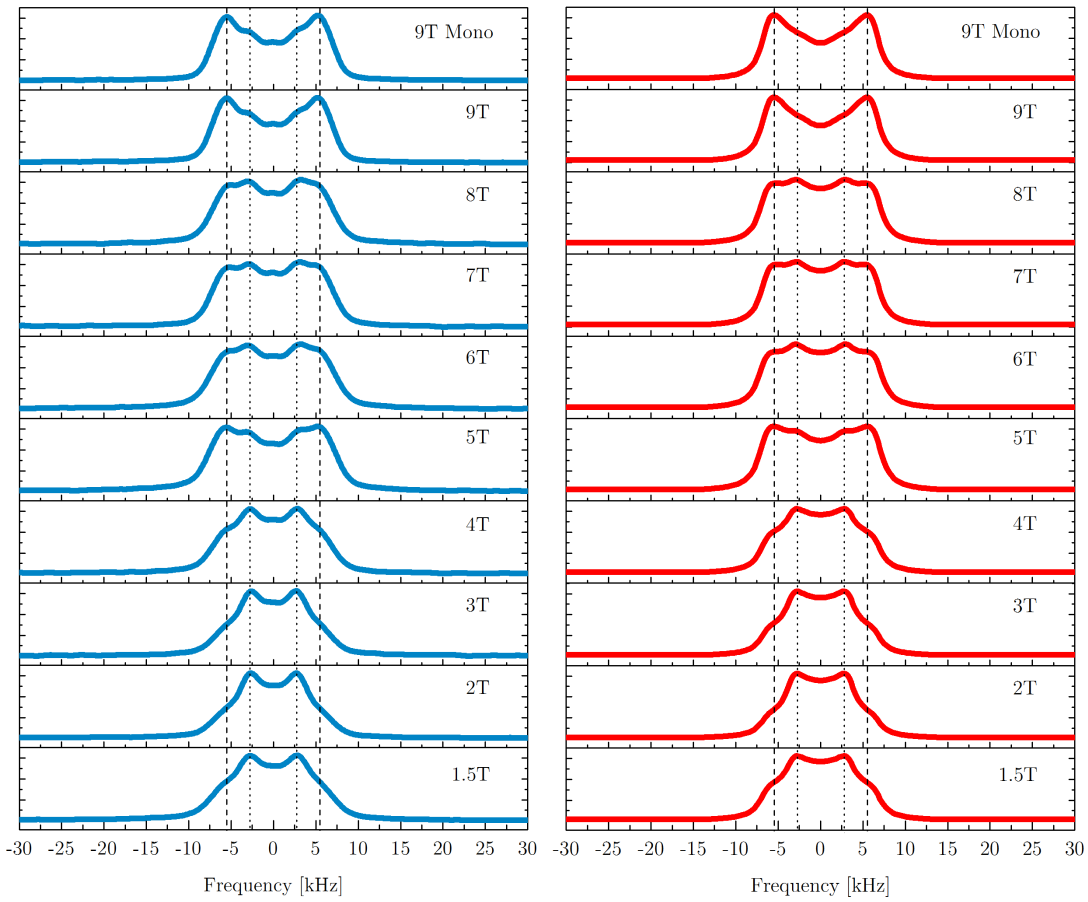


Figure 7.5: Recorded and simulated spectra of PDLCE-Ds. Recorded spectra (blue) exhibit two splittings: at $\nu = \pm 3\,\mathrm{kHz}$, associated with unoriented μLCES, and at $\nu = \pm 6\,\mathrm{kHz}$, at which peaks become more pronounced with better particle alignment against the magnetic field. Measured spectra were simulated (red) to derive the orientational distribution σ_θ, needed for assessment of the order parameter Q. Simulations match the recorded spectra to a maximum of 20% error margin.

inner peaks should altogether vanish when the system is completely ordered, which is not the case for our measurements. This means that some disordering still remains in the composite due to the polydomain nature of μLCEs, the alignment of which is determined by their mean nematic director, or to the close packing of non-uniformly shaped particles (the μLCE concentration is at 50 %wt μLCE fraction) that hinders successful reorientation. The measurement of the composite containing ⋆⋆σ synthesized μLCEs (termed MONO in Figure 7.5) also overrides the suspicion of ⋆B synthesized particles being prevalently multi-domain, and thus non-reorientable, since the spectra at $B = 9\,\mathrm{T}$ match very well.

The dispersion of orientational distribution σ_θ (Figure 7.6 – top graph) needed for the assessment of the order parameter Q is estimated by simulating the recorded spectra. The orientational dispersion changes from $\sigma_\theta \approx 40°$ for small fields to a saturated value of $\sigma_\theta \approx 20°$ for fields above $B = 5\,\mathrm{T}$. From this it can be concluded that the maximum ordering is achieved at $B \geq 5\,\mathrm{T}$. The error bars are determined from the modeling precision of the simulated spectra and were calculated as the difference between the second moments of the recorded and simulated spectral lines. These differ by a maximum of ~ 20% error

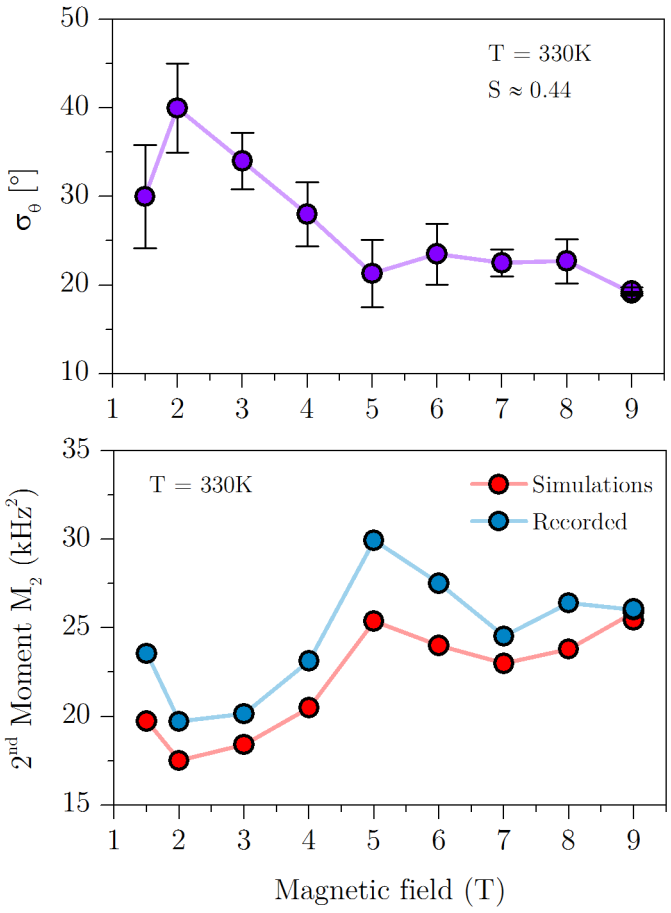


Figure 7.6: Derived orientational distribution σ_θ with associated second moment M_2. μLCEs alignment increases with magnetic field and consequently the orienational distribution σ_θ decreases until it reaches a constant value at $B \geq 5\,\mathrm{T}$, at which point the order parameter reaches its maximum value. Error bars were determined from the difference between the calculated second moments M_2 of recorded and simulated spectra (bottom graph).

margin (see Figure 7.6 – bottom graph). There is a big discrepancy in σ_θ at $B = 1.5\,\mathrm{T}$, which can be attributed to experimental error originating from factors such as different polymerization rates, shape distributions, varied particle concentration, etc. The results for PDLCEs with ⋆B and ⋆⋆σ synthesized μLCEs at $B = 9\,\mathrm{T}$ almost completely overlap, giving again no reason to suspect that different synthesis procedure should affect the results.

The measured orientational distribution σ_θ enables the calculation of the order parameter $Q(\sigma_\theta)$ from Equation (6.9) (Section 7.1). The results shown in Figure 7.7 behave as expected: the calculated order parameter increases with magnetic field until it reaches a constant value at $B = 5\,\mathrm{T}$, where the maximum μLCE alignment is achieved. Some discrepancies are seen at $1.5\,\mathrm{T}$ and $5\,\mathrm{T}$, which are attributed to already explained experimental and fitting error in calculating σ_θ. What is not expected is the low value of the orientational order with the maximum value of $Q_{\max}(\sigma_\theta) \approx 0.54$. These results were simulated (Figure 7.7 – blue line) using a $y = AQ(\tilde{k},\tilde{t})$ function (see Equation (6.16)), derived in the previous section. The simulated functions include an additional constant A, whose purpose is to reduce the maximum value of $Q(\tilde{k},\tilde{t})$ to successfully describe the results. The parameters needed for evaluating $Q(\tilde{k},\tilde{t})$ were calculated using parameters described in Figure 7.4, with magnetic fields in the range $B \in \{0,10\}$. The variable describing the duration of the alignment process t, found in $\tilde{t} = t/\tau$, and constant A were altered to effectively match the results. The best fit was obtained for the values of $A = 0.49$ and $t = 1.2\,\mathrm{min}$, which is also shown in the inset graph in Figure 7.7 where the time evolution of the order parameter Q is calculated for magnetic fields ranging from $9\,\mathrm{T}$ to $1\,\mathrm{T}$ (orange to blue, respectively).

The low values of A and t are to be associated with multiple factors preventing an efficient μLCE alignment. One of the reasons can be the aforementioned polydomain nature

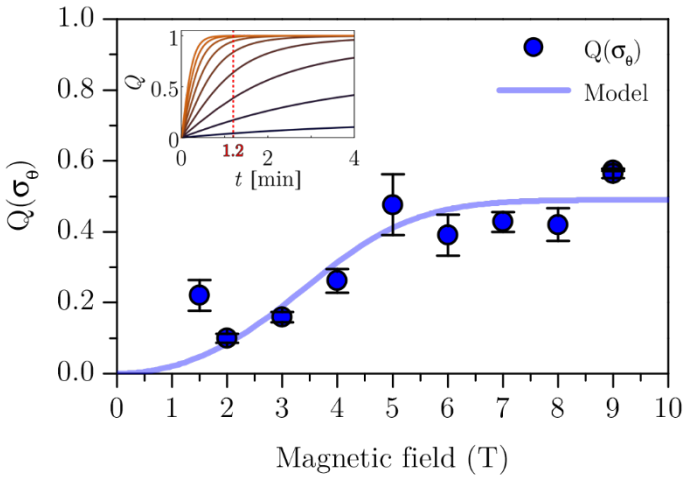


Figure 7.7: Determined order parameter $Q(\sigma_\theta)$. The maximum order parameter is reached for $B \geq 5\,\mathrm{T}$ with the value of $Q_{\max}(\sigma_\theta) \approx 0.54$. Measurements were fitted with $y = AQ(\tilde{k},\tilde{t})$ (blue line), where the constant A describes the maximum order achieved. Parameters $\tilde{k}$ and τ were calculated from determined magnetic fields and known material properties, while the duration of the alignment process, t (found in $\tilde{t} = t/\tau$), and constant A were altered to match the measurements. The best fit was found for $A = 0.49$ and $t = 1.2\,\mathrm{min}$ (graph inset).

of μLCEs, which might not be crushed to a monodomain size, or the particles are forming larger polydomain clusters due to adhesion of monodomain particles during the PDLCE preparation process. But the main cause for low orientational order can be attributed to the DPLCE's high μLCE concentration which was at $50\,\%$wt μLCE fraction. Such high concentrations produce a densely packed environment preventing μLCEs to properly align. Although this value gives the largest TM composite response, it does not mean that the particles are well aligned, since the TM response largely depends on the ratio between the TM inactive PDMS matrix and the TM functionalized LCE material. Even if μLCEs are not completely aligned, the TM response can still be stronger at higher concentrations than at low μLCE proportions of well aligned particles. This can also be the reason for the simulated order parameter's low values for which it seems as though the orientational process is halted at $t = 1.2\,\mathrm{min}$. The model in fact does not take into account the influence of particle concentration, their eventual polydomain nature, and their inhomogeneous size and shape distribution, on the alignment. Nonetheless, it successfully describes the behavior and impact of the matrix's viscosity and magnetic field on the order parameter of PDLCEs. Modeling the recorded spectra of composites with low μLCE concentration could resolve this further and is yet to be performed.

Chapter 8

PDLCE Bilayer Composites

8.1 Morphing of PDLCE Discs

The most important aspect of PDLCEs is the ability to customize their shape-memory behavior, which can go beyond simple contraction and bending of regular LCEs. With PDLCEs there is a possibility to modulate the nematic director orientation of μLCEs throughout their volume in order to achieve different complex shape deformations. Unlike LCEs, PDLCEs can also be molded into arbitrary shapes which widely extends the number of shape-change deformation configurations. In order to demonstrate these facts, two identical PDLCE-A disks with different μLCE orientations (Figure 8.1) were made. In the first case, the nematic director $\mathbf{n}$ is aligned perpendicular to the surface of the disk, $\mathbf{n} \perp \mathbf{Z}$ (Figure 8.1 a), while in the second it is aligned along the surface, $\mathbf{n} \,||\, \mathbf{Z}$ (Figure 8.1 b). Disk preparation procedure is described in Section 8.4.

Upon thermal actuation (raising the temperature above T_{λ}), the resulting disks are deformed accordingly to their director orientation. For $\mathbf{n} \perp \mathbf{Z}$, the thickness of the disk (Z-axis) contracts and the diameter is widened by strain of $\lambda_{X,Y} = \lambda_Z^{-1/2}$ [13] in the $\mathbf{X}$ and $\mathbf{Y}$ direction, thus flattening the sample. The disk with $\mathbf{n} \,||\, \mathbf{Z}$ exhibits a more significantly pronounced shape deformation: the sample is contracted along the $\mathbf{Y}$ direction (see Figure 8.1 b) and expanded in the $\mathbf{X}$ to form an ellipsoid. Both PDLCE deformations are completely reversible and there is no degradation of the TM response with further actuations. The two disks thus act as a simple example of director orientation manipulation capabilities in PDLCEs to achieve different thermally actuated shape changes. Especially the $\mathbf{n} \perp \mathbf{Z}$ director configuration is such that cannot be replicated in regular bulk sized LCEs. By spatially modulating the nematic director $\mathbf{n}$ throughout the PDLCE material, using different directions and/or magnitudes of magnetic field $\mathbf{B}$ or other means, it is possible to assemble different configurations to achieve even more complex shape deformations as will be shown in the next chapter.

8.2 Basic Morphing Configurations Using PDLCE Bilayers

A uniaxial material deformation can still present limitations for many applicative implementations. Even though a homogeneous PDLCE material exhibits only one directional TM deformation, combining them into multiple layers can produce more complex shape changes. Since the pre-polymerized PDLCE melt is a viscous liquid, a multi-layered composite can be created by means of additive manufacturing processes that consist of sequential layer-by-layer deposition and curing of polymer melt. Such processes could be directly utilized for PDLCE production by employing an additional intermediate aligning

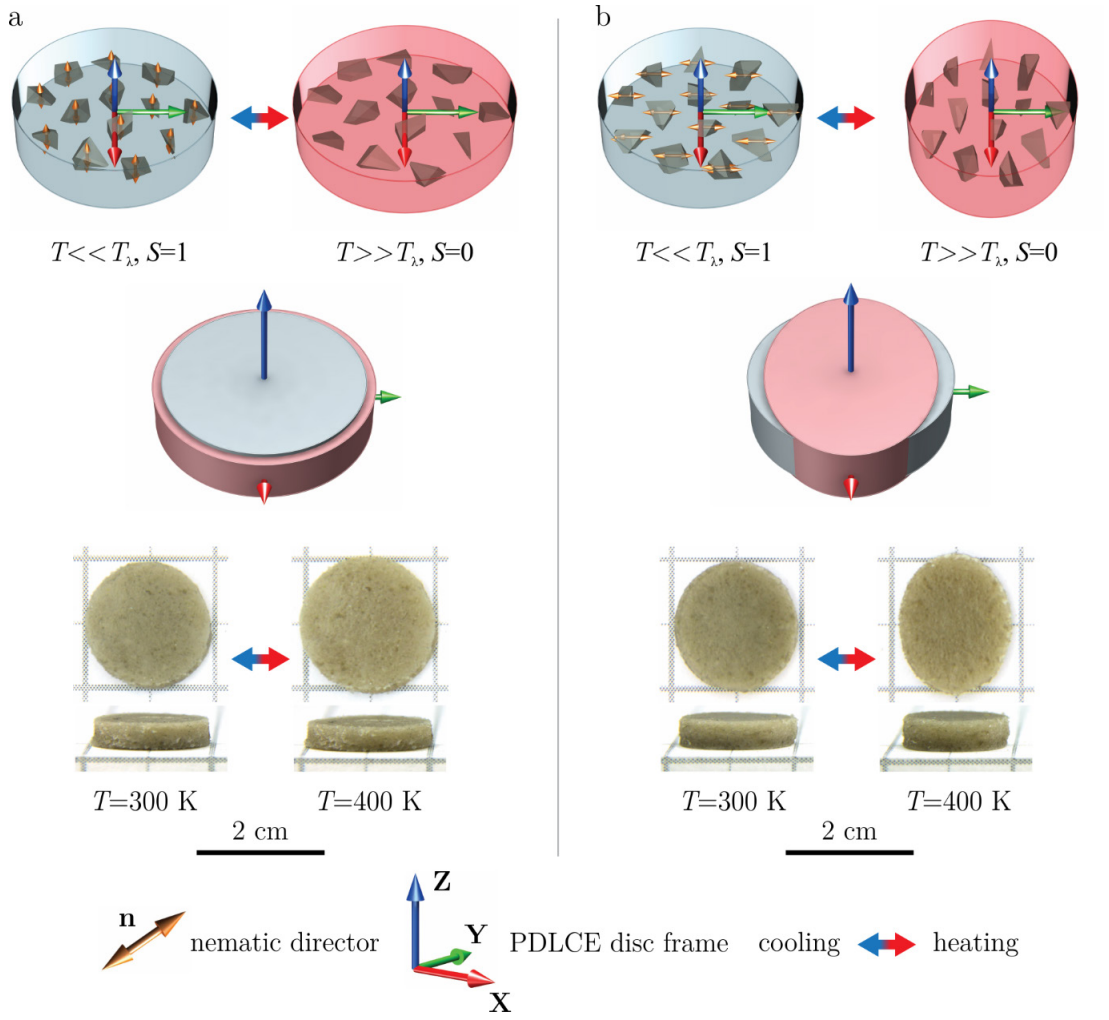


Figure 8.1: TM deformation of disk shaped PDLCEs. Thermal actuation of disk shaped PDLCE-A composites show unique shape changes for different orientations of nematic director $\mathbf{n}$. Illustration depicts the μLCEs orientation for each specimen (top), i.e. 'out of plane' orientation $\mathbf{n} \perp \mathbf{Z}$ (a) and 'in plane' orientation $\mathbf{n} \parallel \mathbf{Z}$ (b), and simulation of consecutive shape changes (middle). The actual disk-shaped composites are shown in bottom photographs. Upon actuation ($T \gg T_\lambda$, $S \to 0$), the 'out of plane' deformation results in a flattened disk, while the 'in plane' orientation disk is morphed into an ellipsoid shape.

step (by means of magnetic or electric field) afore polymerization. To show the morphing abilities gained from layer-by-layer deposition, five PDLCE bilayers were prepared, composed of different combinations of aligned PDLCE material that result in five basic morphing configurations. These can be further combined to achieve a PDLCE composite with arbitrary shape-changing properties.

The basic PDLCE bilayer morphing configurations were named as fold, button, saddle, left twist and right twist configurations (Figure 8.2 a-e, respectively). Composite layers are denoted by subscripts 'b' and 't' for bottom and top layer, respectively, while $Q_{b,t}$ is the layer's order parameter with $Q_{b,t} \neq 0$ meaning that the layer is TM active, otherwise ($Q_{b,t} = 0$) the layer is inert. Relation $\angle \mathbf{n}_{b,t}, \mathbf{Z}$ is the layer's nematic vector alignment against the Z-axis (see Figure 8.2 f) and $\Delta\varphi$ the angle between the top and bottom nematic

directors. A detailed description of each composite's bilayer structure and resulting TM deformation is now given.

The fold configuration is comprised of a functionalized top layer with $\mathbf{n}_t \perp \mathbf{Z}$ and an inert bottom layer ($Q_t \neq 0$ and $Q_b = 0$). Upon thermal activation, the top layer contracts along the nematic director while also pulling the inactive bottom layer up at the sides and thus morphing in a folding manner.

The cup configuration is a combination of a an inactive top layer and TM active bottom layer ($Q_t = 0$ and $Q_b \neq 0$) with $\mathbf{n}_b \,||\, \mathbf{Z}$. Upon activation the bottom layer is flattened (in the $\mathbf{Z}$ direction) with its diameter spontaneously expanding with a larger degree with respect to the smaller linear thermal expansion of the top layer. This difference in layer's

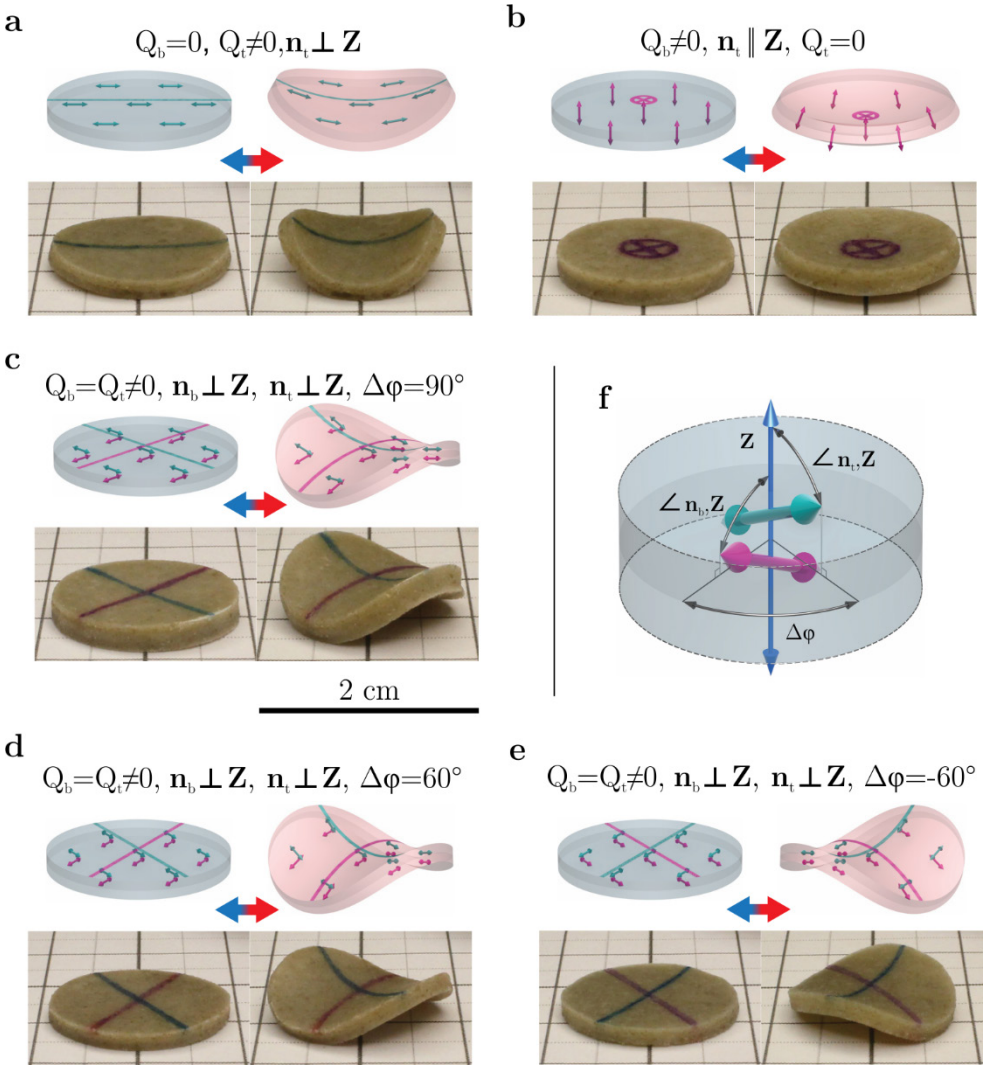


Figure 8.2: Bilayer PDLCE's morphing configurations. Presented are the disk shaped bilayer PDLCE samples that morph into different shapes depending on the TM functionalization of each layer ($Q_{b,t}$), layer's nematic director orientation ($\angle \mathbf{n}_{b,t}, \mathbf{Z}$) and their mutual angle ($\Delta\varphi$). Bottom and top layers are denoted with subscripts 'b' and 't', respectively. Samples are named after their deformation form as followed: fold (a), cup (b), saddle (c), left (d) and right (e) twist. A diagram of the nematic director orientation of each layer and used notations is given in (f).

diameter causes the composite's sides to enclose toward the center, producing a cup-like deformation.

The saddle configuration is, contrary to the fold and cup ones, made out of two functionalized layers ($Q_t \neq 0$ and $Q_b \neq 0$), both with $\mathbf{n}_{b,t} \,||\, \mathbf{Z}$, where the bottom and top nematic directors are perpendicular to each other ($\Delta\varphi = 90°$). Each layer thus contracts along the nematic director, folding the opposite sides upwards at the top layer and downwards at the bottom, which results in a saddle deformation.

The left and the right twist configurations are a version of the saddle configuration, i.e. with both bottom and top layers functionalized ($Q_t \neq 0$ and $Q_b \neq 0$) and $\mathbf{n}_{b,t} \,||\, \mathbf{Z}$, with a difference in the angle between the layer's nematic director alignment, being at $\Delta\varphi = 60°$ for the left twist and $\Delta\varphi = -60°$ for the right twist. The left twist configuration is therefore a mirror of the right twist. Both configurations deform in a similar manner as the saddle resulting in a twist-like deformation at the smaller angle between the layer's nematic directors. The mirroring of directors leads to different twisting deformation directions: counterclockwise for the left twist and clockwise for the right twist. Thus by simply changing the sequence of layer deposition one can instill a mirrored TM actuation of the composite without any sample manipulation.

The above samples were produced to show how one can change the morphing abilities of PDLCE composites by depositing differently oriented layers of TM active and non-active PDLCE material. The five configurations presented can act as five basic voxels in 3D printing technology through which the nematic director can be spatially modulated. There is no doubt that the concept works and therefore PDLCE's employment into the additive manufacturing processes could be relatively simply realized by solely overcoming technical problems arising from customization of existing layer deposition techniques.

8.3 PDLCE Actuator

Customization of PDLCE bilayers is not just limited to multiple layer configurations of changeable TM functionalization and nematic director orientations, but can also be modified using different filler or matrix materials. More specifically, one can accomplish a multiple-stage TM deformation in a single sample by using different μLCEs species for each particular layer. Therefore μLCE-B1 and μLCE-B2, with transition temperatures of $T_{\lambda,1} = 83\,°\mathrm{C}$ and $T_{\lambda,2} = 112\,°\mathrm{C}$ respectively, were used as the filler material for each separate layer and combined them to produce a bilayer PDLCE-B1/B2 composite with PDLCE-B1 as the bottom and PDLCE-B2 as the top layer (Figure 8.3 a).

The nematic director at each layer is oriented perpendicular to the disk's surface (parallel to Z-axis, $\mathbf{n} \,||\, \mathbf{Z}$) so that upon thermal activation of the bottom layer, $T_{\lambda,1} < T < T_{\lambda,2}$, the layer flattens and exhibits the same shape-change as the cup configuration in Figure 8.2. By further increasing the temperature, $T_{\lambda,1} < T_{\lambda,2} < T$, the top layer also deforms with a similar strain, thus pushing down the sides of the disk to acquire the initial non-deformed shape, although with a larger diameter. This kind of PDLCE actuator expresses a shape change only inside a certain temperature interval that leads to a pulse-like deformation behavior. It can also act as an example of how PDLCEs can be assembled into TM valves or pumps that could find its use in multiple applications, such as in microfluidics.

The deformation can also be analyzed by measuring the relative curvature $R_{\min}/R$ of the formed concavity at different temperatures (Figure 8.3 b). With increasing temperature, the relative curvature starts to reduce from the initial flat surface

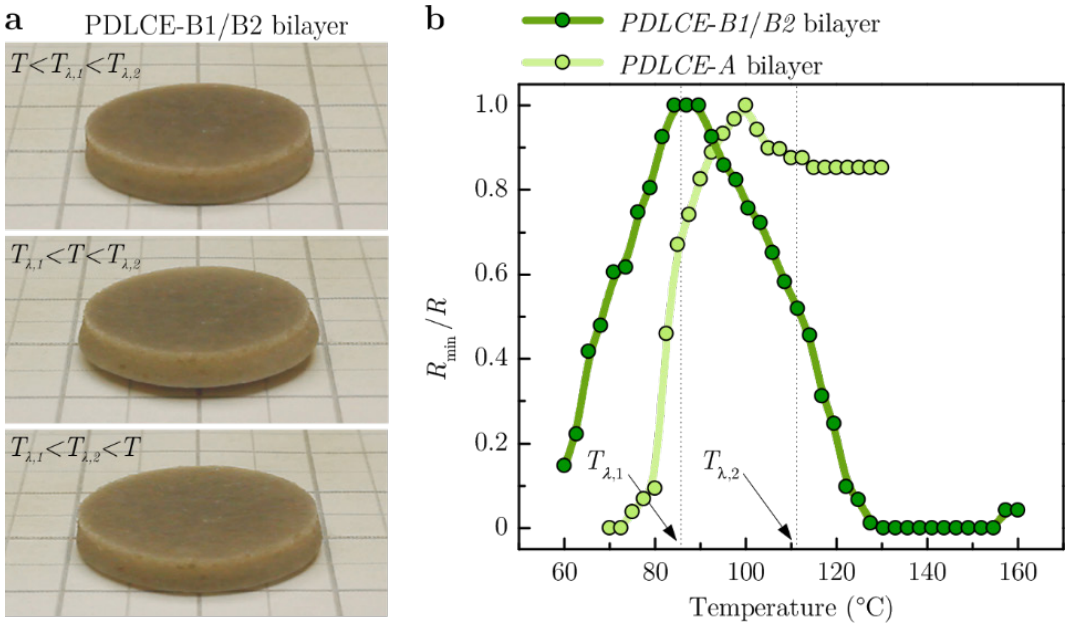


Figure 8.3: PDLCE bilayer actuator. A bilayer PDLCE actuator with each layer composed of different μLCE fillers with differing transition temperatures, $T_{\lambda,1}$ and $T_{\lambda,2}$ and $\mathbf{n} \,||\, \mathbf{Z}$ director orientation. Upon heating, the actuator deforms into a cup when $T_{\lambda,1} < T < T_{\lambda,2}$ and deforms back into disk shape when $T_{\lambda,1} < T_{\lambda,2} < T$ (a), thus morphing only in the specific temperature interval. The TM shape change is analyzed by measuring the relative curvature change R_{min}/R of the composite acquired from photographs (b). The obtained relative curvature (dark green) is compared to the cup configuration (light green) and a two-stage deformation is clearly seen at $T = 83\,°C$ and $T = 112\,°C$ for the actuator, while the cup configuration is deformed only once.

($R \to \infty$) and is maximum at the transition temperature $T_{\lambda,1}$ of the bottom PDLCE-B1 layer, where $R = R_{min}$. By approaching the second transition temperature $T_{\lambda,2}$ of the top PDLCE-B2 layer, the curvature begins to increase, gradually flattening the PDLCE actuator. The relative curvature change is compared to the one obtained for the PLDCE bilayer cup configuration, consisting of only one active layer (PDLCE-A). Here, the composite remains deformed after thermal activation, with its relative curvature reducing only slightly at higher temperatures because of linear thermal expansion of the layers. Nonetheless, the graph clearly depicts how the functionalization of layers with different μLCE species, but with the same bilayer configuration, results in a different shape change deformation and shows yet another way the PDLCE can be customized and fine-tuned to the desired specifications.

8.4 PLDCE Bilayer Preparation

The PDLCE disks were prepared by using a cuboid Teflon mold with a 1 cm in diameter and 2 mm deep cavity on one side, into which the PDLCE-A melt (50 %wt μLCE concentration and $y \approx 0.7$) was poured to fill it completely. A rectangular Teflon foil was used to cover the melt and secured on two sides using Capton® tape, taking care not to introduce air into the cavity. The mold was tightly wrapped with Teflon tape to prevent

the foil coming loose during the curing process. The mold was placed into a $B = 9\,\mathrm{T}$ magnetic field with the sample surface either perpendicular or parallel to the magnetic field, reflecting the desired director orientation. The sample was left at T_{room} for 2 h, for the alignment process to take place, after which it was cured overnight at $T_0 = 50\,^{\circ}\mathrm{C}$.

The PDLCE bilayer composites and actuator were prepared by the same preparation and curing processes as described, except for the use of a different Teflon mold. The rectangular Teflon mold consisted of two cavities of 0.7 mm and 1.4 mm in depth and both with 2 cm radius. PDLCE melt was first poured into the 0.7 mm deep cavity and cured in the desired direction against the magnetic field. Upon the curing process, it was dislodged from the mold and put in the bottom of the 1.4 mm cavity and filled with the remaining melt as the second layer. The nematic director orientation of the cured layer was properly marked beforehand, so that the mold was correctly positioned inside the magnetic field as to the desired composite configuration. For TM inert layers, the mold was simply put in the oven to cure at $T_0 = 60\,^{\circ}\mathrm{C}$.

Chapter 9

Conclusions

The main feature of liquid crystal elastomers is their ability to thermomechanically deform, a property that originates from the orientational characteristics of their mesogenic constituents. Applicative utilization of their TM properties is very much hindered by the complex and impractical synthetization method, which can either yield small-only amounts of micron-sized LCE material of various geometry, or bulk amounts and sizes of LCEs with limited geometry, usually restricted to strip-shaped samples. The research presented in this thesis was focused on overcoming such limitations, therefore a new soft-soft composite material termed Polymer-dispersed liquid crystal elastomers – PDLCEs was developed, comprised of oriented micro-sized LCE particles embedded in a polymer matrix. When a successful coupling between the TM active μLCEs with TM inactive surrounding matrix is achieved, the activated TM response is transferred onto the whole PDLCE composite which deforms in the same manner as its LCE counterpart. Since the PDLCE pre-polymer melt acts as a viscous liquid, it could be applied to many already existing polymer- or elastomer-based industrial production techniques, especially in the now emerging additive manufacturing, such as 3D-printing technology. This means that the PDLCE material can be produced in virtually any shape and size, overcoming the limitations imposed by the use of LCE material.

The material itself is made by freeze-fracturing regular LCE material into micron-sized particles and then dispersing them into the PDMS. The μLCE/PDMS melt is subjected to magnetic field to orient μLCE particles in the field direction by exploiting the mesogen's anisotropic magnetic susceptibility. The melt is then heat-cured at a temperature below the mesogen's nematic to isotropic transition to lock the μLCEs orientation in place. Upon thermal activation, the uniaxial stress induced by μLCE's deformation is exerted onto the surrounding matrix, thus deforming the whole composite.

The orientational degree of μLCEs during the magnetic alignment process is largely determined by the polydomain nature of the LCE material. If the initial LCE material is prepared by the two-step synthesis procedure [9], where the mesogens of a partially crosslinked LCEs are aligned using a mechanical field in the form of a mechanical load, the LCE material expresses a uniform orientational order throughout its volume, rendering it monodomain. μLCEs, acquired from such material, obtain the same monodomain nature, making them well suited for magnetic orientation since they have a well-defined order parameter ($S_N \rightarrow 1$). By omitting the aligning process, the LCE synthetization produces a polydomain material consisting of randomly oriented nematic domains and in turn also yielding polydomain μLCEs ($S_N \approx 0$), if not sufficiently freeze fractured down to their monodomain size. Since bypassing the two-step synthesis procedure would be preferable because of its low yield and impracticality, a synthetization method of LCE material in a strong magnetic field was attempted, which partially aligns the mesogenic constituents

during the synthesis and produces larger oriented nematic domains. Resulting μLCEs could thus exhibit a more defined nematic director ($S_N > 0$). The TM output of PDLCEs comprised of all three μLCEs were measured and compared. The results showed that polydomain μLCEs lead to some degree of PDLCE deformation ($\lambda(T) \approx 1.05$, $\lambda(T) = L(T)/L(T_{ref})$), but they do not match the performance of monodomain two-step synthesized μLCEs with $\lambda(T) \approx 1.12$. Surprisingly, the magnetically synthesized μLCEs exhibit the same amount of deformation as the monodomain μLCEs, meaning that the two-step procedure can be made redundant for PDLCE preparation. A simple synthetization where the LCE melt in arbitrary amounts is crosslinked under a magnetic field can thus be utilized, giving the PDLCEs even more potential for large-scale industrial production.

The amount of PDLCE's deformation depends on the degree of the initial stress of LCE inclusions, its concentration and the elastic constant of both the LCE material and the polymer matrix. The PDLCE's strain output and Young's modulus at different μLCE concentrations and relative elastic constants between the LCE material and the PDMS matrix ($y = E_{LCE}/E_{PDMS}$) were measured to characterize and optimize the composite's TM response. The highest amount of deformation was detected when the μLCE concentration is close to $w_{LCE} \approx 0.50\,\%\text{wt}$ and when the relative elastic constant is $y \leq 1$ ($E_{LCE} \approx E_{PDMS} \approx 90\,\text{kPa}$), i.e. when the LCE material's Young's modulus matches or is lower than the modulus of the polymer matrix. The overall PDLCE elastic constant is also reduced at higher μLCE concentrations and when $y \to 0$, and is mostly governed by the matrix' modulus. The results were simulated with a derived model for calculating the PDLCE's TM response and resulting Young's modulus. A linearly interchanging series and parallel configurations of LCE and PDMS material is presumed in the model, where the parallel scenario is in a rather good agreement with the obtained results.

The degree of μLCE's orientational order parameter Q can be determined with ^{2}H-NMR spectroscopy, where the splitting and the shape of the recorded spectral lines are proportional to the μLCE's mean nematic director orientation against the magnetic field. For this purpose, additional LCE material with deuterium labeled mesogens was synthesized, which enabled the recording of deuterium quadrupole perturbed ^{2}H-NMR spectra. PDLCEs containing the deuterated LCE material were produced and aligned at different magnetic field strengths (from $B = 1.5\,\text{T}$ to $B = 9\,\text{T}$), therefore obtaining composites with different μLCE's orientational order. The recorded spectra were simulated within $20\,\%$ error margin, using a Gaussian-like orientational distribution model to derive the dispersion of orientational distribution σ_θ, associated with the order parameter $Q(\sigma_\theta)$. The results were compared to the calculated order parameter $Q(\tilde{t}, \tilde{k})$, determined by two dimensionless factors, i.e. dimensionless time $\tilde{t} = t/\tau$, which is related to the μLCE's alignment time and factor $\tilde{k}$, describing the polymerization rate of the curing PDMS matrix. The obtained orientational dispersion σ_θ decreases with increasing field, dropping from $\sigma_\theta \approx 40°$ for poorly aligned PDLCEs to a constant value of $\sigma_\theta \approx 20°$ at $B \geq 5\,\text{T}$. The derived order parameter $Q(\sigma_\theta)$ accordingly rises with increasing magnetic field and converges around the maximum value of $Q_{\max}(\sigma_\theta) \approx 0.54$. According to the model's predictions on $Q(\tilde{t}, \tilde{k})$, the maximum value was expected to be higher and to be reached at $B \approx 4\,\text{T}$ at $t > 4\,\text{min}$ into the alignment process. The results were simulated using $y = AQ(\tilde{t}, \tilde{k})$ function, which agrees with the obtained measurements when $A = 0.49$ and $t = 1.2\,\text{min}$, as if the aligning process is instantly stopped at this time. The reasons for such small order parameters are considered to originate from the polydomain nature of μLCEs, their non-uniform size and shape, as well as from the PDLCE's high LCE

particle concentration ($w_{LCE} \approx 0.50\,\%\text{wt}$). These currently non-controlled factors prevent full alignment and may also be responsible for some discrepancies between experiments and model predictions.

PDLCEs have the ability to be customized to achieve different TM responses by simply using different μLCE inclusions. By spatially modulating the orientational order of the particles throughout the composite, they also have the potential to attain custom morphing abilities into a desired shape. Various samples were produced to demonstrate the programmability of PDLCE's TM and morphing abilities. By changing the orientation of μLCEs inside the composites, achieved by aligning disk shaped PDLCEs with either parallel or perpendicularly applied magnetic field to the disk surface, the composites exhibit an 'in-plane' and 'out-of-plane' TM response, respectively, something that cannot be achieved by regular LCEs. Combining differently oriented disk shaped PDLCEs into bilayers produces complex shape-changes through non-matching strains. The resulting five configurations morph into a fold, cup, saddle, and exhibit either a left and right twist deformation. These configurations could also act as five basic voxels in 3D-printing technology to produce a PDLCE-based object with arbitrary shape change. By producing a bilayer with each layer comprised of different species of μLCE inclusions having different transition temperatures, a PDLCE actuator with a beat-like TM response was also made, which morphs into a cup only inside a specific temperature interval. This kind of PDLCEs actuators have a potential to be utilized as valves or TM switches. Due to their practicality and customization capabilities demonstrated in this thesis, it is believed that PDLCEs carry a high potential for use in actuator or other similar applications based on soft matter materials.

References

[1] A. Rešetič, J. Milavec, B. Zupančič, V. Domenici, and B. Zalar, "Polymer-dispersed liquid crystal elastomers," *Nature Communications*, vol. 7, p. 13140, Oct. 2016.

[2] Y. Bar-Cohen, "Electroactive polymer (EAP) actuators for future humanlike robots," 2009, vol. 7287, pp. 728703-728703–6.

[3] M. Warner and E. M. Terentjev, *Liquid Crystal Elastomers*, New Ed edition. St Louis: Oxford University Press, USA, 2007.

[4] J. D. W. Madden *et al.*, "Artificial muscle technology: physical principles and naval prospects," *IEEE Journal of Oceanic Engineering*, vol. 29, no. 3, pp. 706–728, Jul. 2004.

[5] C. Ohm, M. Brehmer, and R. Zentel, "Liquid Crystalline Elastomers as Actuators and Sensors," *Adv. Mater.*, vol. 22, no. 31, pp. 3366–3387, Aug. 2010.

[6] W. H. de Jeu, *Liquid Crystal Elastomers: Materials and Applications*. Springer, 2012.

[7] Z. Pei, Y. Yang, Q. Chen, E. M. Terentjev, Y. Wei, and Y. Ji, "Mouldable liquid-crystalline elastomer actuators with exchangeable covalent bonds," *Nat Mater*, vol. 13, no. 1, pp. 36–41, Jan. 2014.

[8] T. H. Ware, M. E. McConney, J. J. Wie, V. P. Tondiglia, and T. J. White, "Voxelated liquid crystal elastomers," *Science*, vol. 347, no. 6225, pp. 982–984, Feb. 2015.

[9] J. Küpfer and H. Finkelmann, "Nematic liquid single crystal elastomers," *Makromol. Chem., Rapid Commun.*, vol. 12, no. 12, pp. 717–726, Dec. 1991.

[10] H. Zeng, P. Wasylczyk, G. Cerretti, D. Martella, C. Parmeggiani, and D. S. Wiersma, "Alignment engineering in liquid crystalline elastomers: Free-form microstructures with multiple functionalities," *Applied Physics Letters*, vol. 106, no. 11, p. 111902, Mar. 2015.

[11] C. Modes and M. Warner, "Shape-programmable materials," *Physics today*, vol. 69, no. 1, p. 32-, 2016.

[12] S. Palagi *et al.*, "Structured light enables biomimetic swimming and versatile locomotion of photoresponsive soft microrobots," *Nat Mater*, vol. 15, no. 6, pp. 647–653, Jun. 2016.

[13] M. Warner and E. M. Terentjev, *Liquid Crystal Elastomers*. Oxford University Press, USA, 2003.

[14] R. Y. Dong, *Nuclear Magnetic Resonance of Liquid Crystals*, 2nd ed. Springer, 1997.

[15] M. Kleman and O. D. Lavrentovich, *Soft Matter Physics: An Introduction*, 2003rd ed. Springer, 2002.

[16] C. H. Legge, F. J. Davis, and G. R. Mitchell, "Memory effects in liquid crystal elastomers," *Journal de Physique II*, vol. 1, no. 10, p. 9, 1991.

[17] A. Lebar, *NMR Investigations of Monodomain Liquid Crystal Elastomers*. Doctoral Disertation, 2006.

[18] A. Lebar, G. Cordoyiannis, Z. Kutnjak, and B. Zalar, "The Isotropic-to-Nematic Conversion in Liquid Crystalline Elastomers," in *Liquid Crystal Elastomers: Materials and Applications*, W. H. de Jeu, Ed. Springer Berlin Heidelberg, 2010, pp. 147–185.

[19] C. M. Yakacki, M. Saed, D. P. Nair, T. Gong, S. M. Reed, and C. N. Bowman, "Tailorable and programmable liquid-crystalline elastomers using a two-stage thiol–acrylate reaction," *RSC Adv.*, vol. 5, no. 25, pp. 18997–19001, Feb. 2015.

[20] P. L. Sherrell and D. A. Crellin, "SUSCEPTIBILITIES AND ORDER PARAMETERS OF NEMATIC LIQUID CRYSTALS," *Le Journal de Physique Colloques*, vol. 40, no. C3, pp. C3-211-C3-216, Apr. 1979.

[21] A. Buguin, M.-H. Li, P. Silberzan, B. Ladoux, and P. Keller, "Micro-Actuators: When Artificial Muscles Made of Nematic Liquid Crystal Elastomers Meet Soft Lithography," *J. Am. Chem. Soc.*, vol. 128, no. 4, pp. 1088–1089, Feb. 2006.

[22] C. Ohm, N. Haberkorn, P. Theato, and R. Zentel, "Template-Based Fabrication of Nanometer-Scaled Actuators from Liquid-Crystalline Elastomers," *Small*, vol. 7, no. 2, pp. 194–198, Jan. 2011.

[23] J. E. Marshall, S. Gallagher, E. M. Terentjev, and S. K. Smoukov, "Anisotropic Colloidal Micromuscles from Liquid Crystal Elastomers," *J. Am. Chem. Soc.*, vol. 136, no. 1, pp. 474–479, Jan. 2014.

[24] H. Zeng *et al.*, "High-Resolution 3D Direct Laser Writing for Liquid-Crystalline Elastomer Microstructures," *Adv. Mater.*, vol. 26, no. 15, pp. 2319–2322, Apr. 2014.

[25] J. E. Marshall, Y. Ji, N. Torras, K. Zinoviev, and E. M. Terentjev, "Carbon-nanotube sensitized nematic elastomer composites for IR-visible photo-actuation," *Soft Matter*, vol. 8, no. 5, pp. 1570–1574, Jan. 2012.

[26] A. Kaiser, M. Winkler, S. Krause, H. Finkelmann, and A. M. Schmidt, "Magnetoactive liquid crystal elastomer nanocomposites," *J. Mater. Chem.*, vol. 19, no. 4, pp. 538–543, Jan. 2009.

[27] G.-W. Lee, M. Park, J. Kim, J. I. Lee, and H. G. Yoon, "Enhanced thermal conductivity of polymer composites filled with hybrid filler," *Composites Part A: Applied Science and Manufacturing*, vol. 37, no. 5, pp. 727–734, May 2006.

[28] P.-C. Ma *et al.*, "Enhanced Electrical Conductivity of Nanocomposites Containing Hybrid Fillers of Carbon Nanotubes and Carbon Black," *ACS Appl. Mater. Interfaces*, vol. 1, no. 5, pp. 1090–1096, May 2009.

[29] H. Schad, G. Baur, and G. Meier, "Investigation of the dielectric constants and the diamagnetic anisotropies of cyanobiphenyls (CB), cyanophenylcyclohexanes (PCH), and cyanocyclohexylcyclohexanes (CCH) in the nematic phase," *The Journal of Chemical Physics*, vol. 71, no. 8, pp. 3174–3181, Oct. 1979.

[30] M. Doi and S. F. Edwards, *The Theory of Polymer Dynamics*. Clarendon Press, 1988.

[31] T. Kimura, M. Yamato, W. Koshimizu, M. Koike, and T. Kawai, "Magnetic Orientation of Polymer Fibers in Suspension," *Langmuir*, vol. 16, no. 2, pp. 858–861, Jan. 2000.

[32] B. Cowan, *Nuclear Magnetic Resonance and Relaxation*. Cambridge University Press, 2005.

[33] C. P. Slichter, *Principles of Magnetic Resonance*, 3rd enlarged and updated ed. 1990. Corr. 3rd printing 1996 edition. Berlin ; New York: Springer, 1996.

[34] J. Milavec, V. Domenici, B. Zupančič, A. Rešetič, A. Bubnov, and B. Zalar, "Deuteron NMR resolved mesogen vs. crosslinker molecular order and reorientational exchange in liquid single crystal elastomers," *Phys. Chem. Chem. Phys.*, vol. 18, no. 5, pp. 4071–4077, 2016.

[35] V. Domenici, M. Geppi, and C. A. Veracini, "NMR in chiral and achiral smectic phases: Structure, orientational order and dynamics," *Progress in Nuclear Magnetic Resonance Spectroscopy*, vol. 50, no. 1, pp. 1–50, 2007.

[36] J. Emsley, *Nuclear Magnetic Resonance of Liquid Crystals*. Springer Science & Business Media, 2012.

[37] I. M. Daniel and O. Ishai, *Engineering Mechanics of Composite Materials*. Oxford University Press, 1994.

[38] S. Krause, F. Zander, G. Bergmann, H. Brandt, H. Wertmer, and H. Finkelmann, "Nematic main-chain elastomers: Coupling and orientational behavior," *Comptes Rendus Chimie*, vol. 12, no. 1–2, pp. 85–104, Jan. 2009.

[39] B. Zalar, R. Blinc, S. Žumer, T. Jin, and D. Finotello, "Behavior of mesogenic molecules deposited at the alumina-air interface: A deuteron NMR study," *Phys. Rev. E*, vol. 65, no. 4, p. 041703, Mar. 2002.

[40] M. B. Roller, "Characterization of the time-temperature-viscosity behavior of curing B-staged epoxy resin," *Polym Eng Sci*, vol. 15, no. 6, pp. 406–414, Jun. 1975.

[41] F. Schneider, J. Draheim, R. Kamberger, and U. Wallrabe, "Process and material properties of polydimethylsiloxane (PDMS) for Optical MEMS," *Sensors and Actuators A: Physical*, vol. 151, no. 2, pp. 95–99, Apr. 2009.

Bibliography

Publications Related to the Thesis

Journal Articles

[1] A. Rešetič, J. Milavec, B. Zupančič, V. Domenici, and B. Zalar, "Polymer-dispersed liquid crystal elastomers," *Nature Communications*, vol. 7, p. 13140, Oct. 2016.

[2] J. Milavec, V. Domenici, B. Zupančič, A. Rešetič, A. Bubnov, and B. Zalar, "Deuteron NMR resolved mesogen vs. crosslinker molecular order and reorientational exchange in liquid single crystal elastomers," *Phys. Chem. Chem. Phys.*, vol. 18, no. 5, pp. 4071–4077, 2016.

[3] V. Domenici, J. Milavec, A. Bubnov, D. Pociecha, B. Zupančič, A. Rešetič, V. Hamplová, E. Gorecka, and B. Zalar, "Effect of co-monomers' relative concentration on self-assembling behaviour of side-chain liquid crystalline elastomers," *RSC Adv.*, vol. 4, no. 83, pp. 44056–44064, Sep. 2014.

Conference Paper

/

Other Publications (optional)

[1] A. Mertelj, A. Rešetič, S. Gyergyek, D. Makovec, and M. Čopič, "Anisotropic microrheological properties of chain-forming magnetic fluids," Soft Matter, vol. 7, no. 1, pp. 125–131, Dec. 2010.

Biography

The author of this thesis was born in 1985 in Jesenice, Slovenia. He studied Techniques of Measurement in Physics at the Faculty of Mathematics and Physics, University of Ljubljana and graduated in 2010 with diploma titled Anizotropne mikroreološke lastnosti magnetnih tekočin (Anisotropic microrheological properties of chain-forming magnetic fluids). He then attended a master study programme, Nanoscience and Nanotechnologies, at the Jožef Stefan International Postgraduate School and in 2012 successfully defended his Master Thesis titled, Structure and microrheological properties of binary colloids. The same year he entered the Ph.D. program at the Jožef Stefan International Postgraduate School.